Monthly Notices
of the
ROYAL ASTRONOMICAL SOCIETY

MNRAS **433,** 1871–1891 (2013) doi:10.1093/mnras/stt864
Advance Access publication 2013 June 18

Supernova 2012aw – a high-energy clone of archetypal Type IIP SN 1999em

Subhash Bose,[1]★ Brijesh Kumar,[1] Firoza Sutaria,[2] Brajesh Kumar,[1,3] Rupak Roy,[1] V. K. Bhatt,[1] S. B. Pandey,[1] H. C. Chandola,[4] Ram Sagar,[1] Kuntal Misra[1] and Sayan Chakraborti[5]

[1]*Aryabhatta Research Institute of Observational Sciences, Manora Peak, Nainital – 263 002, India*
[2]*Indian Institute of Astrophysics, Block-II, Koramangala, Bangalore – 560034, India*
[3]*Institut d'Astrophysique et de Géophysique, Université de Liège, Allée du 6 Août 17, Bât B5c, 4000 Liège, Belgium*
[4]*Department of Physics, DSB Campus, Kumaun University, Nainital – 263 002, India*
[5]*Institute for Theory and Computation, Harvard–Smithsonian Center for Astrophysics, 60 Garden Street, Cambridge, MA 02138, USA*

Accepted 2013 May 10. Received 2013 April 27; in original form 2013 April 8

ABSTRACT

We present densely sampled *UBVRI*/*griz* photometric and low-resolution (6–10 Å) optical spectroscopic observations from 4 to 270 d after explosion of a newly discovered Type II SN 2012aw in a nearby (∼9.9 Mpc) galaxy M95. The light-curve characteristics of apparent magnitudes, colours, bolometric luminosity and the presence and evolution of prominent spectral features are found to have striking similarity with the archetypal IIP SNe 1999em, 1999gi and 2004et. The early time observations of SN 2012aw clearly detect minima in the light curve of *V*, *R* and *I* bands near 37 d after explosion and this we suggest to be an observational evidence for emergence of recombination phase. The mid-plateau M_V magnitude (-16.67 ± 0.04) lies in between the bright (∼−18) and subluminous (∼−15) IIP SNe. The mass of nickel is $0.06 \pm 0.01\,M_\odot$. The SYNOW modelling of spectra indicate that the value and evolution of the photospheric velocity is similar to SN 2004et, but about ∼600 km s^{-1} higher than that of SNe 1999em and 1999gi at comparable epochs. This trend is more apparent in the line velocities of Hα and Hβ. A comparison of ejecta velocity properties with that of existing radiation-hydrodynamical simulations indicate that the energy of explosion lies in the range 1–2 × 10^{51} ergs; a further comparison of nebular phase [O I] doublet luminosity with SNe 2004et and 1987A indicate that the mass of progenitor star is about 14 to 15 $M_\odot$. The presence of high-velocity absorption features in the mid-to-late plateau and possibly in early phase spectra show signs of interaction between ejecta and the circumstellar matter; being consistent with its early time detection at X-ray and radio wavebands.

Key words: supernovae: general – supernovae: individual: SN 2012aw – supernovae: individual: SN 1999em – supernovae: individual: SN 1999gi – supernovae: individual: SN 2004et – galaxies: individual: NGC 3551.

1 INTRODUCTION

Early time optical spectra of supernovae (SNe) showing strong Balmer lines of H are classified as type II, whereas SNe I show no H lines. Many subtypes have been introduced (Filippenko 1997) and in IIP, the optical light curve remains constant for about hundred days (called the plateau phase) and then decays exponentially, while both IIL and IIb are characterized by linear decline in the light curves after reaching maxima at about 20 d after explosion (Arcavi et al. 2012). The spectra of all these types show strong P-Cygni line profiles, while the type IIb has weak H features initially and at later phases develop prominent He features similar to the Type Ib SNe. Type IIn events show narrow width of H emission lines (Pastorello et al. 2002) which is indicative of interaction between the SN ejecta and the dense circumstellar medium. In addition, there are peculiar Type II events such as SN 1987A which are characterized by long rise time of their light curve (Utrobin & Chugai 2011; Pastorello et al. 2012).

Type II SNe are widely recognized as end stages of massive ($\gtrsim 8\,M_\odot$) zero-age main-sequence stars which end up as core collapse explosions, having retained significant amount of H envelope

★ E-mail: email@subhashbose.com; bose@aries.res.in

before explosion (Burrows 2013). The observed properties derived from the light curve and spectra of SNe provide important clues to the understanding of explosion mechanisms as well as to the nature of progenitor stars (Smartt et al. 2009). The plateau phase of IIP SNe is sustained by cooling down of the shock-heated expanding ejecta by recombination of H while the post-plateau light curve is powered by the radioactive decay of ^{56}Co into ^{56}Fe, which in turn depend upon the amount of ^{56}Ni synthesized during explosion. The observed properties of IIP SNe differ greatly (Hamuy 2003; Smartt et al. 2009), for example, the mid-plateau bolometric luminosity vary by an order of magnitude from $\sim10^{42.5}$ erg s^{-1} for archetypal IIP SN 2004et to $\sim10^{41.5}$ erg s^{-1} for underluminous SN 2005cs. The class of subluminous events (Pastorello et al. 2004, 2009) is also accompanied by lower ejecta velocity during plateau ($\sim$1000 km s^{-1}) and lower luminosity in the light-curve tail owing to small yield of ^{56}Ni ($\sim$2–5 $\times$ 10^{-3} M$_\odot$), in comparison to the normal luminosity IIP SNe 1999em, 2004et with velocities ($\sim$5000 km s^{-1}) and the mass of ^{56}Ni ($\sim$0.1 M$_\odot$). The subluminous IIP events are associated with O–Ne–Mg core originating from lower mass progenitors (8–10 M$_\odot$), while the normal ones originate from iron-core collapse of massive ($>$10 M$_\odot$) progenitors (Fraser et al. 2011; Janka 2012). However, there are cases, i.e. SN 2008in (Roy et al. 2011) and SN 2009js (Gandhi et al. 2013), where a spectroscopically subluminous IIP event show light-curve properties similar to a normal luminosity event.

The stellar evolution models suggest that Type IIP SNe originate from red supergiants having initial masses between 9 and 25 M$_\odot$ having an upper mass cut of 32 M$_\odot$ for solar metallicity stars (Heger et al. 2003); however, the observational constraints are ambiguous and the mass of progenitors recovered from the analysis of pre-explosion archival *Hubble Space Telescope* (*HST*) images for 20 IIP SNe lie in the range 9–17 M$_\odot$ (Smartt et al. 2009), while the hydrodynamical modelling of light curves for a handful of well-studied IIP SNe indicate that they primarily originate from 15 to 25 M$_\odot$ progenitors (Utrobin & Chugai 2009; Bersten, Benvenuto & Hamuy 2011). Some of the problems in inferring physical properties are the lack of good quality data for nearby SNe.

SN 2012aw was discovered on 2012 March 16.9 by Fagotti et al. (2012) in the nearby galaxy M95 ($\sim$10 Mpc) at an *R*-band magnitude of 15. The first non-detection is reported on March 15.27 (Poznanski et al. 2012a) to a 3σ limit of $R \sim 20.7$. Thus, we adopt 2012 March 16.1 (JD = 245 6002.6 $\pm$ 0.8 d) as the time of explosion (0 d) throughout the paper. The spectra obtained at 2 d by Munari, Vagnozzi & Castellani (2012) showed a featureless blue continuum while the subsequent spectra at later phases by Itoh, Ui & Yamanaka (2012) and Siviero et al. (2012) identify the event as young type IIP. The ultraviolet (UV) follow-up observations with Ultraviolet Optical Telescope (UVOT)/*Swift* are done by Bayless et al. (2013) and similar to the optical, they report emergence of plateau in the UV light curve after 27 d. The analysis of pre-explosion archival *HST* images of M95 in the vicinity of SN 2012aw, by two independent groups of researchers indicate that the progenitor was a red superergiant with masses in the range 14–26 M$_\odot$ (Fraser et al. 2012) and 15–20 M$_\odot$ (Van Dyk et al. 2012), respectively. However, by accounting for appropriate extinction laws to the circumstellar and interstellar dust, Kochanek, Khan & Dai (2012) determine that the luminosity of the progenitor star lies between 4.8 and 5.0 dex in solar units and the mass was less than 15 M$_\odot$. SN 2012aw was also detected in X-rays observations with *Swift*/XRT by Immler & Brown (2012) and in radio observations by Stockdale et al. (2012) and Yadav, Chakraborti & Ray (2012) indicating the interaction of ejecta with the circumstellar material (CSM). The early time (17 d) optical spectropolarimetric observations with 8 m European Southern Observatory VLT by Leonard et al. (2012) find the continuum polarization at the level of 0.3 per cent implying substantial asymmetries in the outer ejecta of SN 2012aw.

In this work, we present results from optical photometric (*UBVRI* and/or *griz*) follow-up observations at 45 phases during 4 to 269 d and low-resolution optical spectroscopic observations at 14 phases during 7 to 270 d of SN 2012aw. The paper is organized as follows. In Sections 2.1 and 2.2, we present the photometric and spectroscopic observations, respectively, and a brief description of light curves and spectra. Determination of reddening and extinction is given in Section 3. In Section 4, we analyse light and colour curves, derive bolometric light curves and estimate mass of nickel. In Section 5, we study spectra, evolution of spectral features, the SYNOW modelling and derive velocity of hydrogen envelope and the photosphere. The characteristics of explosion is described in Section 6 and conclusions are presented in Section 7.

We adopt the distance to the host galaxy M95 as 9.9 $\pm$ 0.1 Mpc which is a weighted mean of the three most reliable redshift-independent distance measurements in the literature, i.e. 10 $\pm$ 0.40 Mpc by Freedman et al. (2001) using cepheids; 9.86 $\pm$ 0.14 Mpc by Russell (2002) using Tully–Fisher method and 9.83 $\pm$ 0.13 Mpc by Bose & Kumar (2013) using SN Expanding photosphere method. SN 2012aw occurred in the outskirts of the host galaxy at a deprojected distance of 6.8 kpc, and the oxygen abundance (12+log[O/H]) of the galactic interstellar medium at the position of SN is estimated as 8.8 $\pm$ 0.1 from the radial metallicity gradient relation in M95 given by Pilyugin, Thuan & Vílchez (2006) and this value is close to the solar abundance for oxygen of 8.65 (Asplund et al. 2009). Some basic properties of the host galaxy and SN 2012aw are listed in Table 1.

Table 1. Properties of the host galaxy NGC 3351 and SN 2012aw.

Parameters	Value	Ref.[a]
NGC 3351:		
Type	Sb	1
RA (J2000)	$\alpha = 10^{\rm h}43^{\rm m}57\overset{\rm s}{.}67$	1
Dec. (J2000)	$\delta = 11^\circ42'13\overset{''}{.}0$	1
Abs. magnitude	$M_B = -20.36$ mag	1
Distance	$D = 9.9 \pm 0.1$ Mpc	Section 1
Scale	1 arcsec $\sim$ 48 pc, 1 arcmin $\sim$ 2.9 kpc	
Distance modulus	$\mu = 29.97 \pm 0.03$	
Apparent radius	$r_{25} = 3.6$ arcmin ($\sim$ 10.5 kpc)	1
Inclination angle	$\Theta_{\rm inc} = 54\overset{\circ}{.}6$	1
Position angle	$\Theta_{\rm maj} = 9\overset{\circ}{.}9$	1
Heliocentric velocity	$cz_{\rm helio} = 778 \pm 2$ km s^{-1}	1
SN 2012aw:		
RA (J2000)	$\alpha = 10^{\rm h}43^{\rm m}53\overset{\rm s}{.}73$	2
Dec. (J2000)	$\delta = 11^\circ40'17\overset{''}{.}9$	
Galactocentric location	58 arcsec W, 115 arcsec S	
Deprojected radius	$r_{\rm SN} = 139.1$ arcsec ($\sim$6.75 kpc)	
Time of explosion	t_0 =16.1 March 2012 (UT) (JD 2456002.59)	Section 1
Reddening	$E(B-V) = 0.074 \pm 0.008$	Section 3

[a](1) HyperLEDA – Paturel et al. (2003).
(2) Van Dyk et al. (2012).

2 OBSERVATION AND DATA REDUCTION

2.1 Photometry

The broad-band photometric data in *UBVRI* Johnson–Cousins and *griz* SDSS systems are collected using the 104-cm Sampurnanand Telescope (ST) at Manora Peak, Nainital and the 130-cm Devasthal Fast Optical Telescope (DFOT) at Devasthal, Nainital. Both the telescopes are operated by the Aryabhatta Research Institute of Observational Sciences, India (Sagar, Kumar & Omar 2013). The 104-cm ST is equipped with a 2k × 2k liquid-nitrogen cooled CCD camera having square pixels of 24 μm and with a plate scale of 0.37 arcsec per pixel, the CCD covers a square field of view of about 13 arcmin on a side in the sky. While operating at 27 kHz, the gain and readout noise of the CCD are $10e^-$ per analogue-to-digital unit (ADU) and $5.3e^-$, respectively. The 130-cm DFOT is equipped with a 2k × 2k Peltier-cooled CCD camera having a pixel size of 13.5 μm and with a plate scale of 0.54 arcsec per pixel, the CCD covers a square field of view of 18 arcmin on a side. The CCD was operated at 31 kHz speed with readout noise of $2.5e^-$ – a detailed technical description and performance of this camera can be found elsewhere (Sagar et al. 2012). A binning of 2 × 2 is used in CCDs wherever required to improve the signal-to-noise ratio (SNR). At 104-cm ST, we had *UBVRI* while at 130 cm, we had *BVR* as well as *griz* filters. A typical exposure time of 300 s was given for *U* and *B* filters while 80–200 s was given for remaining filters. For *V* band, the full width at half-maximum (FWHM) of the stellar point spread function (PSF) varied between 2.1 and 3.5 arcsec, with a median value of 2.6 arcsec. In addition to the target exposures, several bias and twilight flat frames are also obtained for calibration purpose.

The bias subtraction, flat fielding, cosmic ray removal, alignment and determination of mean FWHM and ellipticity for each object frames are done using the standard tasks available in the data reduction softwares IRAF[1] and DAOPHOT.[2] Whenever multiple frames are available, the photometry is performed on co-added frames. As the location of SN is fairly isolated from the galaxy centre and it lies on a smooth and faint galaxy background (see Fig. 1), we chose to perform aperture photometry, and an aperture radius equal to the mean FWHM of a given frame and a 10 pixel wide sky annulus at 6 FWHM radius were chosen. This whole scheme of aperture photometry is achieved using stand alone version of DAOPHOT subroutines. The differential instrumental magnitude for each filter was generated using DAOMASTER task.

In order to calibrate instrumental magnitude of SN 2012aw , the Landolt (2009) standard fields PG 1323, PG 1525 and PG 1633 were observed on 2012 March 22 in *UBVRI* filters with the 104-cm ST under photometric night conditions viz. transparent sky and FWHM seeing in $V \sim 2$ arcsec. The observations of standard fields were taken at five locations covering airmass from 1.06 to 2.36. The SN field is also observed on the same night. The data reduction of SN and Landolt fields is done using profile fitting technique and the instrumental magnitudes were converted into standard system following least-squares linear regression procedures outlined in Stetson (1992), in which zero-points, colour coefficients and the atmospheric extinction coefficients are fitted simultaneously for 17 stars having *V* magnitude from 12.0 to 16.4 and $B - V$ from −0.22 to 1.14 mag. The root-mean-squared (rms) scatter between the transformed and the standard magnitudes of Landolt stars is found to be ∼0.04 mag in *U*, 0.02 mag in *B* and 0.01 mag in *VRI*. The transformation coefficients were used to generate local standard stars in the field of SN 2012aw observed on the same night and a set of 11 stars with *V* range from 12 to 17 mag and $B - V$ range of 0.36 to 1.06 mag were selected. These stars are identified in Fig. 1 and are listed in Table 2. The quoted errors include both photometric and calibration errors propagated in quadrature. The frame-to-frame photometric variability of these stars during 4 to 269 d was found to lie within quoted uncertainties.

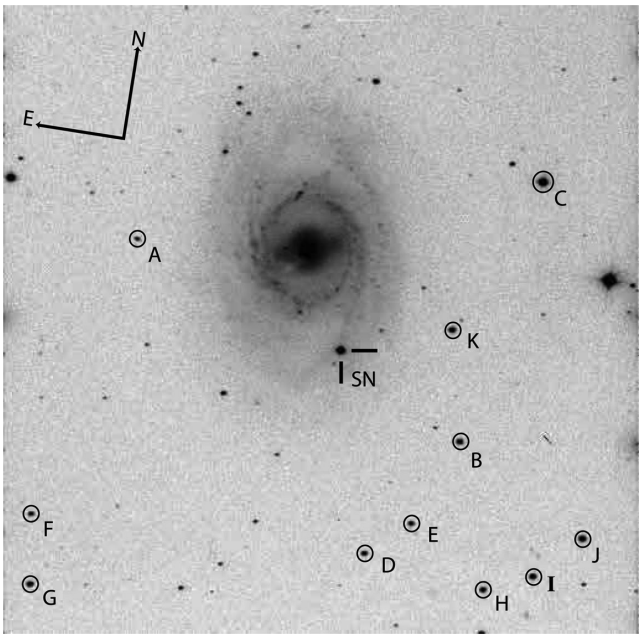

Figure 1. SN 2012aw in NGC 3551. The *V*-band image taken from 104 cm ST covering an area of about 13 arcmin × 13 arcmin is shown. The location of SN and local standard stars are marked.

Four of these stars are in common with the study of Henden, Krajci & Munari (2012) who provided calibrated *BVRI* magnitudes of 14 stars in 20 arcmin × 20 arcmin field of SN 2012aw. A comparison with their photometry gives a mean and rms scatter of -0.04 ± 0.04, -0.01 ± 0.03, 0.02 ± 0.04 and 0.00 ± 0.03 mag, respectively, for *B*, *V*, *R* and *I*, indicating that the two photometric measurements are consistent within uncertainties. The magnitude of local standards in *griz* were taken from Lupton et al. (2005).

The final photometry of SN 2012aw is given in Table 3.

2.2 Spectroscopy

During 7 to 270 d, long-slit low-resolution spectra in the optical range were collected at 14 epochs; nine from 2 m IUCAA Girawali Observatory (IGO) telescope and five from 2 m Himalayan Chandra Telescope (HCT). Journal of spectroscopic observations is given in Table 4. Observations at 2 m IGO have been carried out using IUCAA Faint Object Spectrograph and Camera (IFOSC) mounted at the Cassegrain focus of f/10 reflector (Gupta et al. 2002; Chakraborty, Das1 & Tandon 2005). Grism 5 ($\lambda \sim 0.33$–0.63 μm; $\Delta\lambda \sim 8.8$ Å) and pair of grism 7 and 8 ($\lambda \sim 0.38$–0.83 μm; $\Delta\lambda \sim 4$ Å) along with a slit width of 1.5 arcsec are used to record spectra on 2048 × 2048 E2V CCD with 13.5 μm pixel size; having a gain of 1.5 e^- per ADU and readout noise of 4 e^-. Calibration frames

[1] IRAF stands for Image Reduction and Analysis Facility distributed by the National Optical Astronomy Observatories which is operated by the Association of Universities for research in Astronomy, Inc., under cooperative agreement with the National Science Foundation.

[2] DAOPHOT stands for Dominion Astrophysical Observatory Photometry (Stetson 1987).

Table 2. Identification number (ID), coordinates (α, δ) and calibrated magnitudes of stable secondary standard stars in the field of SN 2012aw. The field of SN 2012aw was calibrated using Landolt standards observed on the night of 2012 March 22. The quoted errors in magnitude include both photometric and calibration errors and it denote 1σ uncertainty.

Star ID	α_{J2000} ($^{h\,m\,s}$)	δ_{J2000} ($^{\circ}\,'\,''$)	U (mag)	B (mag)	V (mag)	R (mag)	I (mag)
A	10:44:11.82	+11:41:54.5	18.168 ± 0.078	17.650 ± 0.045	16.775 ± 0.057	16.316 ± 0.024	15.841 ± 0.017
B	10:43:42.70	+11:38:51.1	15.801 ± 0.024	15.611 ± 0.008	14.897 ± 0.011	14.493 ± 0.013	14.049 ± 0.016
C	10:43:39.17	+11:44:21.3	13.774 ± 0.014	12.882 ± 0.007	11.878 ± 0.026	11.358 ± 0.035	10.866 ± 0.035
D	10:43:49.09	+11:36:17.4	16.277 ± 0.024	16.179 ± 0.012	15.522 ± 0.017	15.139 ± 0.021	14.748 ± 0.019
E	10:43:45.65	+11:37:02.8	16.804 ± 0.037	16.453 ± 0.012	15.668 ± 0.013	15.243 ± 0.016	14.817 ± 0.022
F	10:44:17.02	+11:36:02.1	16.540 ± 0.026	16.760 ± 0.012	16.399 ± 0.014	16.123 ± 0.026	15.795 ± 0.016
G	10:44:16.18	+11:34:37.0	16.277 ± 0.031	15.687 ± 0.015	14.851 ± 0.014	14.397 ± 0.019	13.966 ± 0.018
H	10:43:38.86	+11:35:56.5	16.160 ± 0.023	15.919 ± 0.012	15.207 ± 0.016	14.818 ± 0.020	14.453 ± 0.023
I	10:43:34.96	+11:36:22.2	15.746 ± 0.022	15.494 ± 0.009	14.787 ± 0.012	14.406 ± 0.025	13.966 ± 0.016
J	10:43:31.33	+11:37:17.7	15.954 ± 0.018	14.955 ± 0.006	13.896 ± 0.013	13.300 ± 0.025	12.712 ± 0.016
K	10:43:44.75	+11:41:04.4	15.190 ± 0.020	15.328 ± 0.009	14.944 ± 0.009	14.727 ± 0.012	14.467 ± 0.014

Table 3. Photometric evolution of SN 2012aw. Errors denote 1σ uncertainty.

UT date (yy/mm/dd)	JD 245 6000+	Phase[a] (d)	U (mag)	B (mag)	V (mag)	R (mag)	I (mag)	Tel[b]	Seeing[c] (arcsec)
2012-03-19.82	006.32	4	12.671 ± 0.042	13.504 ± 0.021	13.574 ± 0.017	13.463 ± 0.018	13.433 ± 0.025	ST	2.6
2012-03-20.80	007.30	5	12.582 ± 0.042	13.492 ± 0.021	13.478 ± 0.017	13.372 ± 0.018	13.325 ± 0.025	ST	2.3
2012-03-21.81	008.31	6	12.517 ± 0.042	13.457 ± 0.021	13.420 ± 0.012	13.300 ± 0.018	13.258 ± 0.018	ST	2.0
2012-03-22.76	009.26	7	12.599 ± 0.042	13.415 ± 0.021	13.380 ± 0.017	13.262 ± 0.018	13.239 ± 0.025	ST	2.0
2012-03-24.84	011.34	9	12.652 ± 0.042	13.394 ± 0.021	13.340 ± 0.017	13.175 ± 0.018	13.132 ± 0.025	ST	1.9
2012-03-25.78	012.28	10	12.676 ± 0.043	13.411 ± 0.021	13.328 ± 0.017	13.192 ± 0.014	13.130 ± 0.025	ST	2.3
2012-04-01.63	019.13	17	13.010 ± 0.042	13.567 ± 0.021	13.318 ± 0.017	13.089 ± 0.018	12.990 ± 0.025	ST	2.2
2012-04-07.63	025.13	23	13.627 ± 0.043	13.756 ± 0.021	13.325 ± 0.017	13.073 ± 0.018	12.923 ± 0.025	ST	2.2
2012-04-09.74	027.24	25	13.909 ± 0.042	13.875 ± 0.021	13.351 ± 0.017	13.086 ± 0.018	12.950 ± 0.025	ST	2.3
2012-04-12.71	030.21	28	14.199 ± 0.042	14.000 ± 0.021	13.366 ± 0.017	13.111 ± 0.018	12.940 ± 0.025	ST	2.4
2012-04-19.65	037.15	35	14.788 ± 0.043	14.228 ± 0.021	13.439 ± 0.017	13.140 ± 0.018	12.918 ± 0.025	ST	2.5
2012-04-21.61	039.11	37	14.905 ± 0.043	14.284 ± 0.021	13.468 ± 0.017	13.151 ± 0.018	12.895 ± 0.018	ST	2.9
2012-04-22.82	040.32	38	–	–	13.493 ± 0.017	13.135 ± 0.018	12.899 ± 0.052	ST	2.7
2012-04-25.75	043.25	41	15.189 ± 0.044	14.392 ± 0.021	13.463 ± 0.017	13.124 ± 0.018	12.851 ± 0.025	ST	2.1
2012-04-29.70	047.20	45	15.377 ± 0.050	14.466 ± 0.021	13.487 ± 0.017	13.126 ± 0.018	12.836 ± 0.025	ST	2.8
2012-05-01.61	049.11	47	15.455 ± 0.057	14.491 ± 0.025	13.725 ± 0.024	13.115 ± 0.023	12.887 ± 0.035	ST	2.9
2012-05-04.63	052.13	50	15.552 ± 0.089	–	13.439 ± 0.018	13.115 ± 0.018	12.776 ± 0.055	ST	2.1
2012-05-06.62	054.12	52	15.725 ± 0.041	14.574 ± 0.021	13.471 ± 0.017	13.116 ± 0.018	12.790 ± 0.052	ST	2.4
2012-05-08.61	056.11	54	–	–	13.526 ± 0.018	13.113 ± 0.019	12.812 ± 0.026	ST	2.7
2012-05-09.61	057.11	55	15.802 ± 0.067	14.688 ± 0.024	13.494 ± 0.017	13.088 ± 0.018	12.775 ± 0.025	ST	2.9
2012-05-11.65	059.15	57	–	14.518 ± 0.022	13.534 ± 0.017	13.085 ± 0.018	–	DFOT	3.1
2012-05-13.68	061.18	59	16.049 ± 0.059	14.697 ± 0.021	13.539 ± 0.017	13.097 ± 0.018	12.804 ± 0.025	ST	2.6
2012-05-14.69	062.19	60	16.133 ± 0.068	14.711 ± 0.022	13.566 ± 0.017	13.139 ± 0.018	12.797 ± 0.025	ST	2.6
2012-05-17.64	065.14	63	16.239 ± 0.049	14.771 ± 0.021	13.556 ± 0.017	13.102 ± 0.018	12.774 ± 0.025	ST	2.8
2012-05-24.63	072.13	70	16.424 ± 0.089	14.817 ± 0.021	13.571 ± 0.017	13.106 ± 0.018	12.787 ± 0.025	ST	3.1
2012-05-27.66	075.16	73	16.577 ± 0.144	14.882 ± 0.022	13.596 ± 0.018	13.118 ± 0.018	12.778 ± 0.025	ST	2.9
2012-05-27.65	075.15	73	–	14.611 ± 0.023	13.596 ± 0.012	13.110 ± 0.018	–	DFOT	2.8
2012-05-28.63	076.13	74	–	14.609 ± 0.025	13.637 ± 0.018	13.115 ± 0.018	–	DFOT	3.1
2012-05-30.65	078.15	76	–	14.872 ± 0.031	13.627 ± 0.018	13.126 ± 0.018	12.786 ± 0.025	ST	3.8
2012-06-06.64	085.14	83	16.840 ± 0.061	14.990 ± 0.021	13.687 ± 0.017	13.127 ± 0.018	12.804 ± 0.018	ST	3.4
2012-06-09.62	088.12	86	17.010 ± 0.062	15.042 ± 0.022	13.664 ± 0.017	13.174 ± 0.018	12.828 ± 0.025	ST	2.5
2012-06-11.63	090.13	88	16.886 ± 0.052	15.057 ± 0.021	13.670 ± 0.017	13.159 ± 0.018	12.815 ± 0.025	ST	2.8
2012-06-16.66	095.16	93	–	14.694 ± 0.029	13.727 ± 0.018	13.206 ± 0.013	–	DFOT	3.3
2012-06-25.65	104.15	102	–	15.231 ± 0.029	13.873 ± 0.022	13.361 ± 0.023	12.995 ± 0.031	ST	3.7
2012-06-27.63	106.13	104	16.979 ± 0.219	15.158 ± 0.018	13.824 ± 0.017	13.296 ± 0.018	12.947 ± 0.025	ST	3.7
2012-10-16.96	217.46	215	–	17.526 ± 0.083	16.577 ± 0.025	15.794 ± 0.020	–	DFOT	3.5
2012-10-17.96	218.46	216	–	17.657 ± 0.053	16.617 ± 0.024	15.823 ± 0.014	–	DFOT	3.5
2012-10-23.98	224.48	222	–	18.069 ± 0.361	16.918 ± 0.366	–	15.413 ± 0.059	ST	3.4
2012-10-24.97	225.47	223	–	18.033 ± 0.026	16.711 ± 0.019	15.832 ± 0.019	15.368 ± 0.026	ST	2.2
2012-10-26.97	227.47	225	–	18.106 ± 0.023	16.730 ± 0.019	15.860 ± 0.019	15.389 ± 0.026	ST	2.7
2012-10-29.99	230.49	228	–	–	16.667 ± 0.015	–	–	ST	1.7
2012-10-30.98	231.48	229	19.551 ± 0.361	18.088 ± 0.038	16.765 ± 0.020	15.899 ± 0.014	15.447 ± 0.025	ST	1.8
2012-11-02.97	234.47	232	–	18.163 ± 0.030	16.803 ± 0.020	15.949 ± 0.011	15.454 ± 0.026	ST	2.0

Table 3 – *continued*

UT date (yy/mm/dd)	JD 245 6000+	Phase[a] (d)	*U* (mag)	*B* (mag)	*V* (mag)	*R* (mag)	*I* (mag)	Tel[b]	Seeing[c] (arcsec)
2012-11-04.96	236.46	234	–	18.126 ± 0.030	16.841 ± 0.016	15.975 ± 0.020	15.456 ± 0.026	ST	2.0
2012-11-07.97	239.47	237	–	18.278 ± 0.078	16.721 ± 0.046	15.955 ± 0.031	15.454 ± 0.040	ST	2.2
2012-11-10.95	242.45	240	–	17.850 ± 0.051	16.911 ± 0.022	15.992 ± 0.019	–	DFOT	2.9
2012-11-11.94	243.44	241	–	17.875 ± 0.051	16.963 ± 0.021	15.996 ± 0.019	–	DFOT	3.0
2012-11-16.98	248.48	246	20.291 ± 0.239	18.264 ± 0.019	16.908 ± 0.014	16.039 ± 0.019	15.586 ± 0.019	ST	2.0
2012-11-18.98	250.48	248	19.934 ± 0.153	18.289 ± 0.020	16.927 ± 0.018	16.054 ± 0.019	15.610 ± 0.026	ST	1.7
2012-11-25.95	257.45	255	19.821 ± 0.111	18.323 ± 0.018	17.011 ± 0.014	16.132 ± 0.019	15.709 ± 0.026	ST	1.9
2012-12-04.90	266.40	264	–	18.325 ± 0.060	17.051 ± 0.040	16.012 ± 0.036	15.726 ± 0.050	ST	2.0
2012-12-04.86	266.36	264	–	–	17.130 ± 0.071	–	–	DFOT	3.0
2012-12-09.02	270.52	268	–	18.415 ± 0.070	17.109 ± 0.022	16.225 ± 0.020	15.811 ± 0.026	ST	2.6
2012-12-09.98	271.48	269	20.166 ± 0.165	18.429 ± 0.022	17.113 ± 0.019	16.242 ± 0.019	15.837 ± 0.026	ST	2.2
			g (mag)	*r* (mag)	*i* (mag)	*z* (mag)			
2012-05-11.66	059.16	57	13.922 ± 0.031	13.242 ± 0.028	13.187 ± 0.021	13.185 ± 0.070		DFOT	3.1
2012-05-27.68	075.18	73	14.038 ± 0.031	13.259 ± 0.028	13.199 ± 0.021	13.164 ± 0.049		DFOT	2.8
2012-05-28.65	076.15	74	14.052 ± 0.031	13.269 ± 0.028	13.192 ± 0.021	13.172 ± 0.070		DFOT	3.1
2012-06-16.67	095.17	93	14.173 ± 0.031	13.326 ± 0.028	13.259 ± 0.021	13.192 ± 0.070		DFOT	3.3
2012-10-16.97	217.47	215	17.150 ± 0.033	15.948 ± 0.028	15.907 ± 0.022	15.376 ± 0.071		DFOT	3.5
2012-10-17.98	218.48	216	17.161 ± 0.033	15.971 ± 0.028	15.914 ± 0.022	15.399 ± 0.071		DFOT	3.5
2012-11-10.93	242.43	240	17.339 ± 0.033	16.171 ± 0.028	16.158 ± 0.022	15.570 ± 0.071		DFOT	2.9
2012-11-11.93	243.43	241	17.353 ± 0.033	16.173 ± 0.028	16.167 ± 0.022	–		DFOT	3.0
2012-12-04.95	266.45	264	–	–	–	–		DFOT	3.0

[a]With reference to the explosion epoch JD 245 6002.59.
[b]ST: 104-cm Sampurnanand Telescope, ARIES, India; DFOT : 130-cm Devasthal fast optical telescope, ARIES, India.
[c]FWHM of the median stellar PSF at *V*-band frame.

Table 4. Journal of optical spectroscopic observations of SN 2012aw. The spectral observations are made at 14 phases between 7 and 270 d.

UT date (yy/mm/dd.dd)	JD 245 6000+	Phase[a] (d)	Range[b] (μm)	Telescope[c]	Grating (gr mm^{-1})	Slit width (arcsec)	Dispersion (Å pix^{-1})	Exposure (s)	S/N[d] (pix^{-1})
2012-03-22.752	9.25	7	0.38–0.68	HCT	600	1.92	1.43	900	85
			0.58–0.84	HCT	600	1.92	1.26	900	66
2012-03-23.768	10.26	8	0.33–0.63	IGO	300	1.50	2.75	900	147
2012-03-27.615	14.12	12	0.38–0.68	HCT	600	1.92	1.49	1200	123
			0.58–0.84	HCT	600	1.92	1.26	900	75
2012-03-30.659	17.16	15	0.38–0.68	HCT	600	1.92	1.49	900	91
			0.58–0.84	HCT	600	1.92	1.26	900	68
2012-03-31.809	18.30	16	0.38–0.68	HCT	600	1.92	1.49	900	48
			0.58–0.84	HCT	600	1.92	1.26	900	35
2012-04-04.714	22.21	20	0.38–0.68	HCT	600	1.92	1.61	1200	127
			0.58–0.84	HCT	600	1.92	1.25	1200	86
2012-04-10.715	28.21	26	0.38–0.68	IGO	600	1.50	1.39	2700	112
			0.58–0.83	IGO	600	1.50	1.16	1200,2104	71
2012-04-15.802	33.30	31	0.33–0.63	IGO	300	1.50	2.89	1800x2	171
2012-04-29.685	47.18	45	0.33–0.63	IGO	300	1.50	2.89	1200x2	114
2012-05-09.713	57.22	55	0.38–0.68	HCT	600	1.92	1.61	1200	139
			0.58–0.84	HCT	600	1.92	1.25	1200	104
2012-05-15.680	63.19	61	0.38–0.68	IGO	600	1.50	1.38	1800	103
			0.58–0.83	IGO	600	1.50	1.16	1800	85
2012-05-20.730	68.23	66	0.38–0.68	HCT	600	1.92	1.61	900	95
			0.58–0.84	HCT	600	1.92	1.25	900	64
2012-06-27.629	106.13	104	0.38–0.68	HCT	600	1.92	1.61	1200	56
			0.58–0.84	HCT	600	1.92	1.25	1200	38
2012-12-10.846	272.37	270	0.38–0.68	HCT	600	1.92	1.43	2400	26
			0.58–0.84	HCT	600	1.92	1.26	2400	20

[a]With reference to the burst time JD 245 6002.59.
[b]For transmission ≥50 per cent.
[c]HCT: HFOSC on 2 m Himalyan Chandra Telescope, Hanle; IGO: IFOSC on 2 m IUCAA Girawali Observatory, India.
[d]At 0.6 μm.

(bias, flat, HeNe arc) and spectrophotometric flux standard stars (Feige34, Hr4468 and Hz44) were observed on each night. Observations from 2 m HCT have been carried out in similar fashion with HFOSC using pair of grisms 7 and 8 ($\lambda \sim 0.38$–0.84 μm; $\Delta\lambda \sim 4$ Å) and a slit width of 1.92 arcsec. For flux calibration, stars Feige66, Feige110 and Grw70d5824 are observed and FeAr and FeNe arcs are observed for wavelength calibrations.

Spectroscopic data reduction was done under IRAF environment. Bias and flat fielding were performed on each frames. Cosmic ray rejection on each frame was done using Laplacian kernel detection algorithm for spectra, L.A.COSMIC (van Dokkum 2001). One-dimensional spectra were extracted using *APALL* task which is based on optimal extraction algorithm by Horne (1986). Wavelength calibration was performed using *identify* task and about 15–18 emission lines of HeNe (for IGO) or FeNe and FeAr (for HCT) were used to find dispersion solution. The position of O I emission skyline at 5577 Å was used to check the wavelength calibration and deviations were found to lie between 0.3 and 5.5 Å and this was corrected by applying a linear shift in wavelength. The instrumental FWHM resolution of 2 m IGO spectra as measured from O I 5577 Å emission skyline was found to lie between ∼6 and 12 Å (∼317–671 km s^{-1}) and that of 2 m HCT was found to lie between ∼8 and 10 Å.

The flux calibration of wavelength-calibrated spectra was done using *STANDARD*, *SENSFUNC* and *CALIBRATE* tasks. We used spectrophotometric standard fluxes from Oke (1990) and Hamuy et al. (1994), and the spectral extinction coefficients from Stalin et al. (2008) and Chakraborty et al. (2005) for the respective sites. All the spectra were tied to an absolute flux scale using zero-points determined from *UBVRI* magnitudes. To tie the spectra with photometry, the individual spectrum is multiplied by wavelength-dependent polynomial function and its *BVRI* filter response convolved fluxes are compared with photometric fluxes at corresponding epoch. The multiplied polynomial is tuned to minimize the flux difference and obtain the tied spectrum. The one-dimensional spectra are corrected for heliocentric velocity of the host galaxy (778 km s^{-1}; Section 1) using *DOPCOR* tasks.

3 EXTINCTION

In order to derive intrinsic properties of explosion, the reddening due to interstellar matter in both the Milky Way and the host galaxy towards the sight line of SN 2012aw should be known accurately. Using all-sky dust-extinction map of Schlegel, Finkbeiner & Davis (1998), we derived the value of Galactic reddening as $E(B-V)_{\rm MW} = 0.0278 \pm 0.0002$ mag. The reddening due to host galaxy $E(B-V)_{\rm host}$ was estimated using two methods viz. the blackbody approximations to the 4 d fluxes and the narrow blended Na I doublet absorption lines in the spectra.

The observed spectral energy distribution (SED) of a few days old SNe can be approximated as a blackbody and hence, we generated observed spectral fluxes between 0.26 and 0.81 μm, using photometric data at 4 d in $uvw1$ band ($\lambda_c = 2600$ Å) of *Swift* UVOT taken from Bayless et al. (2013) and in *UBVI* bands from the present study. The 4 d data for UVOT filters $uvw2$ ($\lambda_c = 1928$ Å) and $uvm2$ ($\lambda_c = 2246$ Å) are not used because of higher errors and also we did not rely on *R* flux because of the high contamination due to Hα emission. In Fig. 2, we have plotted the dereddened observed fluxes for varying $E(B-V)$ and here, the dereddening is done using reddening law of Cardelli, Clayton & Mathis (1989) for a total-to-selective extinction ratio ($R_{\rm V}$) of 3.1. We also show the corresponding blackbody model fluxes with best-fitting temperatures, and corresponding to $E(B-V)$ of 0.028 mag, we derive a temperature of 14.2 kK. For $E(B-V) = 0.25$ mag, we obtain an unphysical high temperature of 32 kK. The theoretical modelling of Dessart & Hillier (2006) and Bersten et al. (2011) indicate that a value of temperature above 20kK is not expected for 4 d old Type IIP SNe and hence we derive an upper limit for total $E(B-V)$ of 0.15 mag.

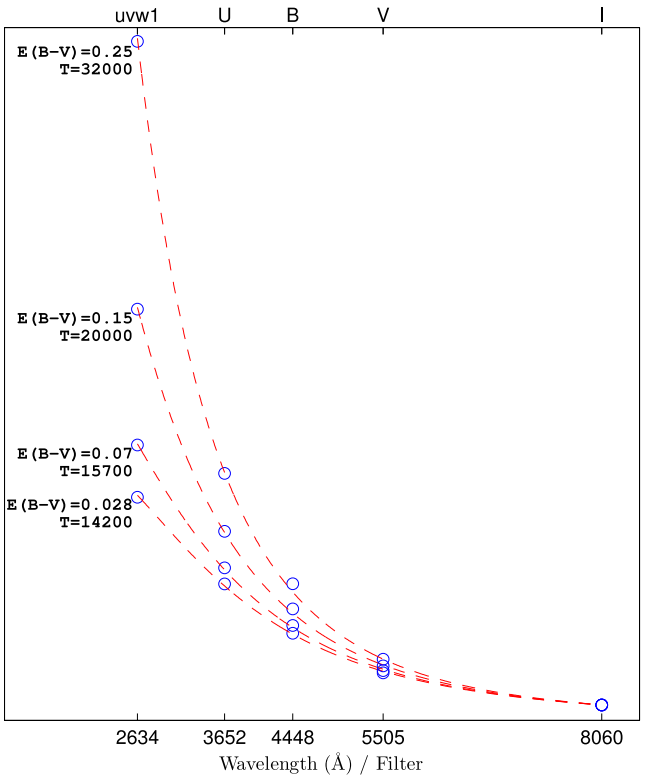

Figure 2. The SED of SN 2012aw at 4 d is compared with blackbody function. The open circles denote observed fluxes in $uvw1$, *U*, *B*, *V* and *I* bands corrected for respective reddening values while the dotted lines are the best-fitting models for different temperatures. The fluxes are normalized relative to *I*-band flux.

The equivalent width (EW) of Na I D absorption feature is found to be correlated with the reddening $E(B-V)$ estimated from the tail of SN Ia colour curves (Barbon et al. 1990; Turatto, Benetti & Cappellaro 2003), though it may be a bad proxy in certain cases, e.g. see Poznanski et al. (2011). In the low-resolution spectra presented in this work, it is not possible to resolve the individual component of Na I doublet (D_1 5889.95 Å and D_2 5895.92 Å) and hence we can expect to see the blended feature at the gf-weighted rest wavelength of 5893 Å. At all the 14 phases of spectra, a weak impression of Na I D due to the host is seen overlaid on the broad P-Cygni profile due to SN (see Fig. 3), whereas the feature due to Milky Way is comparatively weak and it is visible only for spectra with high SNR. In Table 5, we list the EW of Na I D due to host galaxy only and no attempt is made to estimate EW due to Milky Way. Due to poor SNR (<50; Table 4), the 16, 104 and 270 d spectra were not included in the EW determination. The error in EW is calculated using the relation given by Vollmann & Eversberg (2006) for weak-line limit. The weighted mean of EW derived from 11 individual measurements is 0.394 ± 0.067 Å. Employing empirical relation from Poznanski, Prochaska & Bloom (2012b), i.e. $\log_{10}E(B-V)_{\rm host} = 1.17 \times {\rm EW} - 1.85 \pm 0.08$ (where EW in Å), a value of 0.041 ± 0.011 mag is obtained for reddening due to host galaxy and the error quoted here includes both that in EW and that in the empirical relation. This value is consistent with the $E(B-V)_{\rm host} = 0.055 \pm 0.014$ mag,

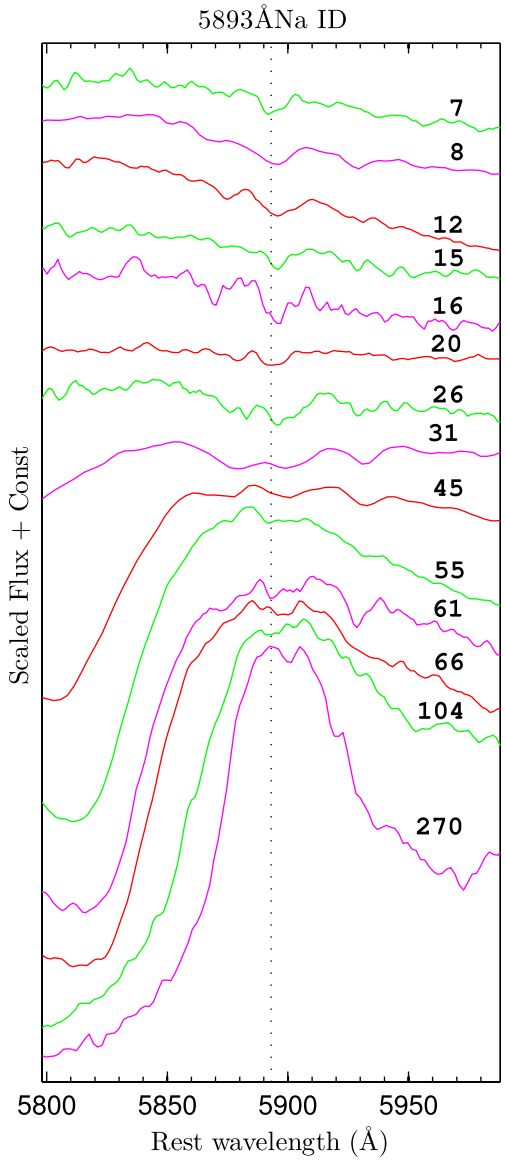

Figure 3. The Na I D blended feature due to host galaxy at around 5893 Å is shown by dotted line.

Table 5. EWs of Na I D absorption feature due to host galaxy.

UT date (yyyy-mm-dd)	Phase[a] (d)	EW (Å)
2012-03-22	7	0.415 ± 0.204
2012-03-23	8	0.410 ± 0.185
2012-03-27	12	0.400 ± 0.233
2012-03-30	15	0.374 ± 0.361
2012-04-04	20	0.399 ± 0.172
2012-04-10	26	0.370 ± 0.226
2012-04-15	31	0.364 ± 0.189
2012-04-29	45	0.413 ± 0.276
2012-05-09	55	0.363 ± 0.237
2012-05-15	61	0.419 ± 0.233
2012-05-20	66	0.400 ± 0.272
Weighted mean		0.394 ± 0.067

[a]With reference to the time of explosion JD 245 46002.59.

which is derived by Van Dyk et al. (2012) using high-resolution echelle spectra of SN 2012aw obtained from 10 m Keck telescope at 25 d. We derive a weighted mean of the above two measurements, i.e. 0.046 ± 0.008 mag for the host galaxy and by adding the Galactic reddening, a total $E(B-V)_{\rm tot} = 0.074 \pm 0.008$ mag is derived for SN 2012aw and is adopted throughout this paper. This corresponds to a visual extinction $A_V = 0.23 \pm 0.03$ mag, assuming line-of-sight ratio of total-to-selective extinction $R_{\rm V} = 3.1$.

4 OPTICAL LIGHT CURVE

4.1 Apparent magnitude light curves

The optical light curve of SN 2012aw in *UBVRI* filters is shown in Fig. 4. The photometric measurements are made at 54 phases during 4 to 269 d. The SDSS *griz* magnitudes are converted to *BVRI* using empirical relations given by Jordi, Grebel & Ammon (2006) and are overplotted. For comparison the light curves of archetypal Type IIP SN 1999em (Leonard et al. 2002a) are also shown. The early light curve shows sharp initial rise of brightness in all the optical bands and then declines slowly into the plateau phase followed by a sharp fall at around 110 d to the nebular phase. On the contrary, the observations in UVOT bands do not show any initial rise in the light curve observed since as early as 3 d (Bayless et al. 2013). The peak in early time light curve occurs at about 8, 11, 15, 22 and 24 d, respectively, for *UBVRI* bands, followed by a continuous decline in *UB* and a short decline, and then a continuous rise in *VRI* peaking at 52, 56 and 71 d, respectively (see inset in Fig. 4). The early time light curve of SN 2012aw is almost similar to other nearby (≤11 Mpc), well-studied normal Type IIP SNe, e.g. in SN 1999em – *UBV* peaked at 6, 8 and 10 d (Leonard et al. 2002a); in SN 2004et, *UBVRI* peaked at 9, 10, 16, 21 and 25 d (Sahu et al. 2006); and in SN 1999gi, *BV* peaked at 8 and 12 d (Leonard et al. 2002b). Appearance of initial peaks in *UBVRI* seems to be a generic feature of early time light curves of IIP SNe and in the absence of early time data, it can provide a good handle on estimating the time of explosion with accuracy of a few days, e.g. at *V* band, the initial peak occurs at 13 ± 3 d for well-studied IIP SNe. Unlike other SNe, the densely sampled light curve of SN 2012aw offers the opportunity to see, for the first time, the minima near 42 d in *V*, 39 d in *R*, 31 d in *I* band and then a slow rise to a plateau at about 51, 59 and 73 d, respectively. The change in flux from initial early time rise to the minima is about 16 per cent (∼0.18 mag) in *V*, 6 per cent (∼0.07 mag) in *R* and 2 per cent (∼0.02 mag) in *I*. We note that these values are larger than the typical photometric errors at these epochs. This observed minima around which the SN cools down to hydrogen recombination temperature ∼6000 K most likely marks the tail- end of the flux from the adiabatic cooling phase of the shock breakout and the dominance of the flux from the hydrogen recombination phase in the SN envelope (Kasen & Woosley 2009; Cowen, Franckowiak & Kowalski 2010; Roy et al. 2011). However, a dense coverage of this early time data for more number of events would be required to confirm the nature and exact cause of this rebrightening in the light curves.

As the SN goes behind the sun, we have a data gap of 105 to 214 d; however, a prolonged plateau phase of about 100 d is apparently seen. The decline rates up to 104 d after maxima in *UBV* are 5.60, 1.74, 0.55 mag 100 d^{-1}, respectively, which are similar to the values observed for SN 1999em (see Fig. 4) and SN199gi (Leonard et al. 2002b). The rate of decline for SN 2004et is a bit higher, e.g. at B-band it is 2.2 mag 100 d^{-1}. During the plateau phase, *R*-band light curve shows almost no change in brightness,

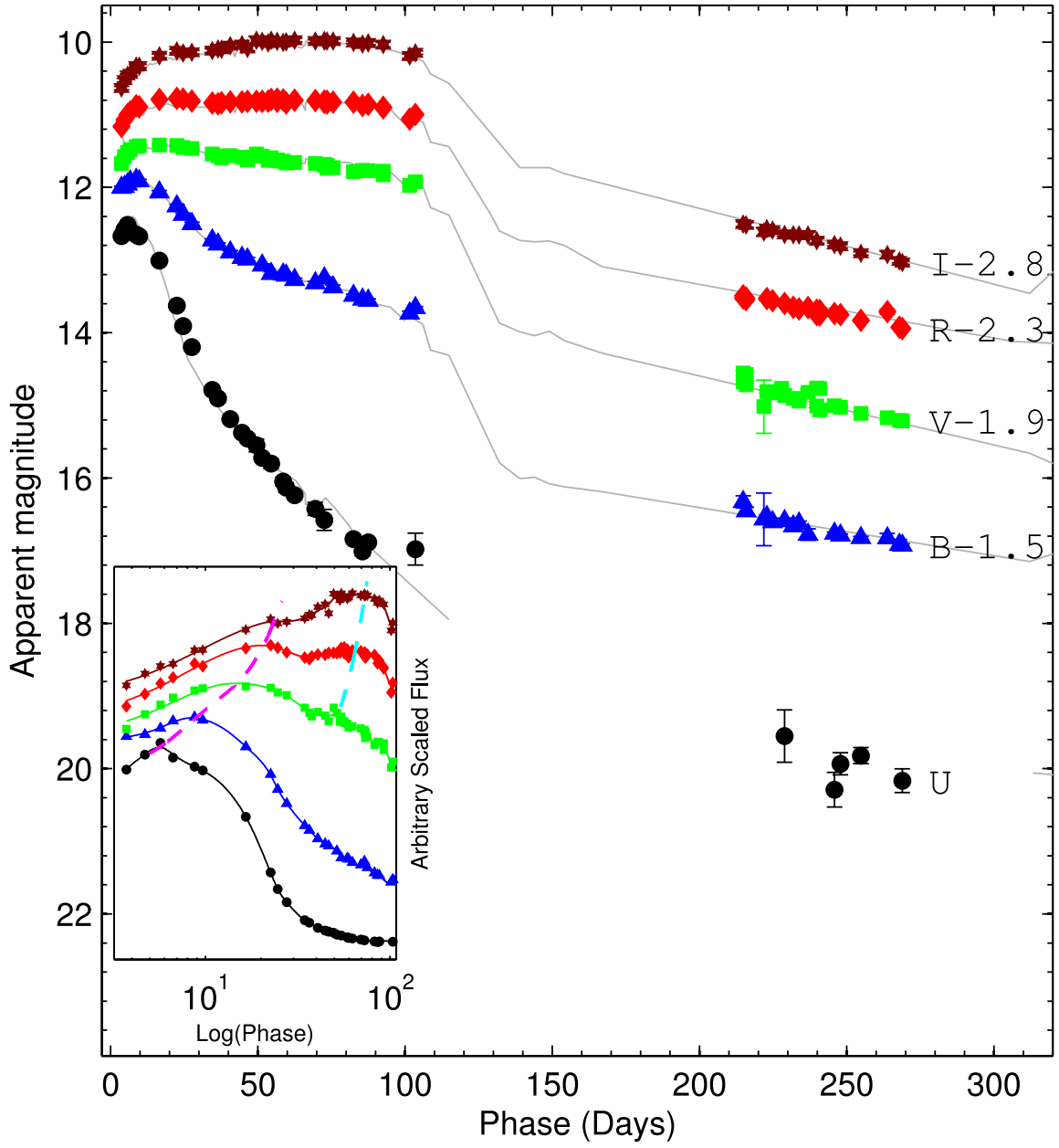

Figure 4. The photometric light curve in Johnson–Cousins *UBVRI* system. The light curves are shifted for clarity, while for SN 1999em (grey solid lines), it is scaled in magnitude to match with SN 2012aw. The evolution of early time light curve is shown in inset, wherein, the primary peaks in *U*, *B*, *V*, *R* and *I* at 6, 9, 14, 20 and 23 d, respectively; and the secondary peak in *V*, *R* and *I* at 52, 56, and 71 d, respectively, are clearly visible. Primary and secondary peaks of the light curve are connected by pair of dashed lines (magenta and cyan, respectively).

whereas the *I* band shows slow increase in brightness until a mid-plateau of ∼60 d, then it remains almost constant until the end of the plateau. The decline rate (mag 100 d^{-1}) in light curve of the nebular phase between 215 and 269 d is estimated as 1.24, 0.88, 0.88, 0.81, and 0.95, respectively, for *UBVRI*.

4.2 Absolute magnitude and colour evolution

After correcting for distance and extinction (Section 3; Table 1), the absolute magnitude *V*-band light curve is shown in Fig. 5 and it is compared with other well-studied SNe of normal type IIP 1999em, 2004et, 1999gi, 2004dj; subluminous type IIP 2005cs and peculiar type II 1987A. The *V*-band light curves of SNe from the literature are also corrected for distance and extinction and the time of explosion for all (except SN 2004dj) of them is known with an accuracy of a day. The comparison shows striking similarity with SN 1999em in both shape and flux. If we ignore the effect of distance, then the duration of the plateau, the nebular phase luminosity and the overall shape of light curve are similar for SNe 1999em, 1999gi and 2012aw; in contrast to that seen for SNe 2005cs and 2004et. For SN 2012aw the plateau-to-nebular phase transition occurs at ∼117 d and the mid-plateau M_V^p is −16.66 mag and hence it belongs to a normal type IIP events (Patat et al. 1994), in contrast to the subluminous IIP like 2005cs with $M_V^p \sim -15$ mag (Pastorello et al. 2009). The peak absolute magnitude of SN 2012aw is equal to that of SN 1999em, about 0.31 mag brighter than SN 1999gi and about 0.49 mag fainter than SN 2004et. The light-curve evolution in the nebular phase follows the decay rate 0.92 mag 100 d^{-1}. The

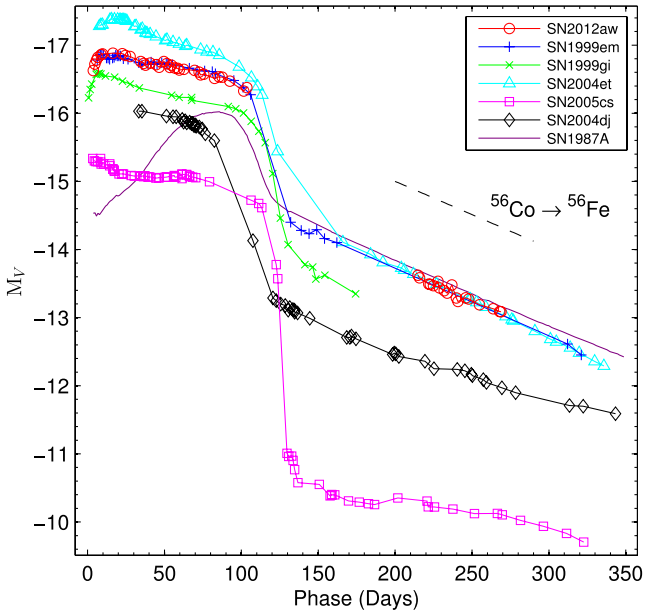

Figure 5. Comparison of M_V light curve of SN 2012aw with other Type IIP SNe. The exponential decline of the radioactive decay law is shown with dashed lines. The time of explosion in JD 240 0000, distance in Mpc, reddening $E(B-V)$ in mag and the reference for apparent V-band magnitude, respectively, are: SN 1999em – 51475.6, 11.7, 0.10; Leonard et al. (2002a); Elmhamdi et al. (2003); SN 2004et – 53270.5, 5.4, 0.41; Sahu et al. (2006); SN 2005cs – 53549.0, 7.8, 0.11; Pastorello et al. (2009); SN 2004dj – 53187.0, 3.5, 0.07; Tsvetkov, Goranskij & Pavlyuk (2008); SN 1987A – 46849.8, 0.05, 0.16; Hamuy & Suntzeff (1990); SN 1999gi – 51522.3, 13.0, 0.21; Leonard et al. (2002b).

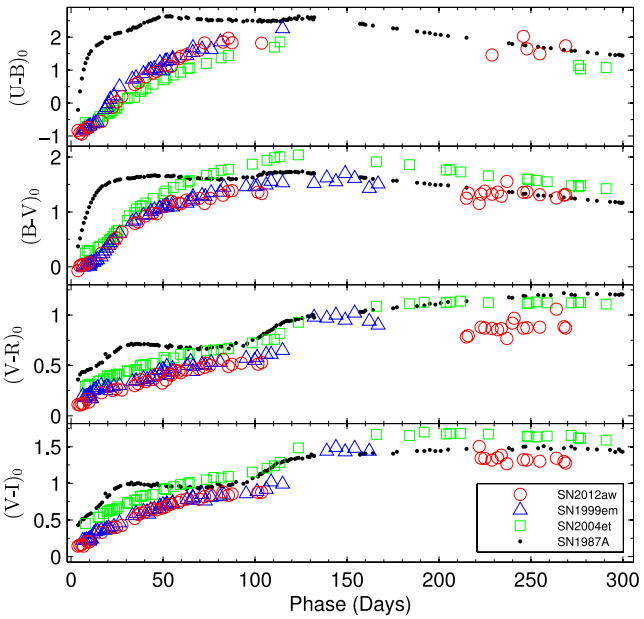

Figure 6. The evolution of intrinsic colours of SN 2012aw is compared with other well-studied normal Type IIP SNe 1999em, 1999gi and 2004et. The references for the data are same as in Fig. 5.

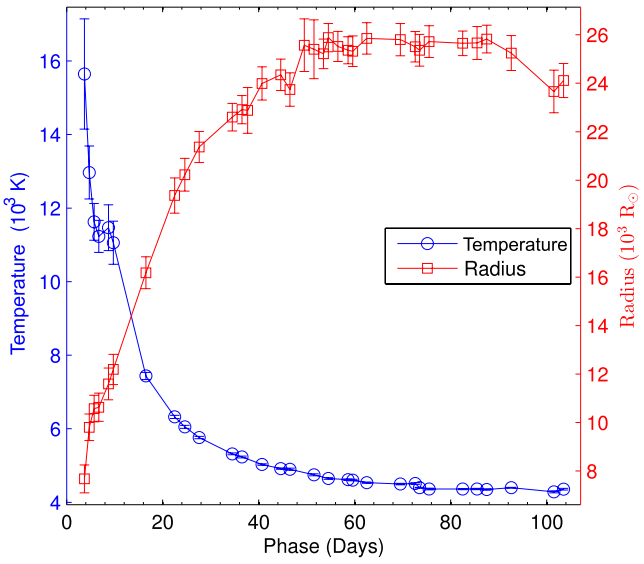

Figure 7. The temperature and radius of SN 2012aw as derived from blackbody fits to the observed fluxes in the UV–optical range 0.17–0.88 μm.

photometric evolution of Type IIP SNe in nebular phase is powered by the radioactive decay of ^{56}Co into ^{56}Fe and the expected decay rate is 0.98 mag 100 d^{-1}. The values for SN 2012aw are consistent with this.

The evolution of broad-band colours provides important clues for the expansion and cooling behaviour of the SN envelope. In Fig. 6, the evolution of intrinsic colours $U-B$, $B-V$, $V-R$ and $V-I$ are shown. The $U-B$ colour evolves very rapidly in early phases up to ∼50 d, primarily due to high temperature and rapid cooling; and it becomes redder from −0.94 to 1.11 mag; though it evolves slowly thereafter and reaches 1.96 mag by 90 d. By 260 d, it becomes blue again by 0.6 mag in about 150 d. The $B-V$ also evolves similar to $U-B$, and in nebular phases both colours follow the evolution completely similar to SN 1987A. The evolution in all the colours shows striking resemblance to that of SN 1999em. The $V-I$, $V-R$ and $B-V$ colours of SN 2012aw are significantly (∼0.2–0.8 mag) bluer than that of SN 2004et at all phases, while the $U-B$ colour is observed to be redder.

In order to have an idea on the temporal evolution of temperature, we fitted blackbody on the observed fluxes in $uvw1$ band (data taken from Bayless et al. 2013) and in *UBVRI* bands covering the wavelength region 0.26–0.81 μm. The $uvm2$ and $uvw2$ bands are not used as these have large uncertainties in magnitudes and also they result in unrealistic blackbody fits at early phases. The fluxes were corrected for interstellar extinction and we also applied dilution factors as per the prescription by Dessart & Hillier (2006). The fitted values of temperature and the radius are plotted in Fig. 7. The blackbody temperature (T_{bb}) thus derived can be approximated as a photospheric temperature. During the phases 4–10 d, the ejecta temperature drops from 16 to 11 kK and by 20 d it drops down to about 6500 K, with a very slow decline thereafter to 4300 K by 104 d. This indicates that the plateau seen in the absolute magnitude light curve between ∼20 and 104 d is mainly sustained by the recombination of hydrogen. The sharp change in slope of T_{bb} around 20–30 d is consistent with the similar trend seen in the colour-curve evolution of $U-B$ and $B-V$.

4.3 Bolometric light curve

The bolometric light curves provide constraint on the amount of radioactive ^{56}Ni synthesized during explosion as well as on the energy of SN explosion. At early phases (≤30 d), when SN ejecta is

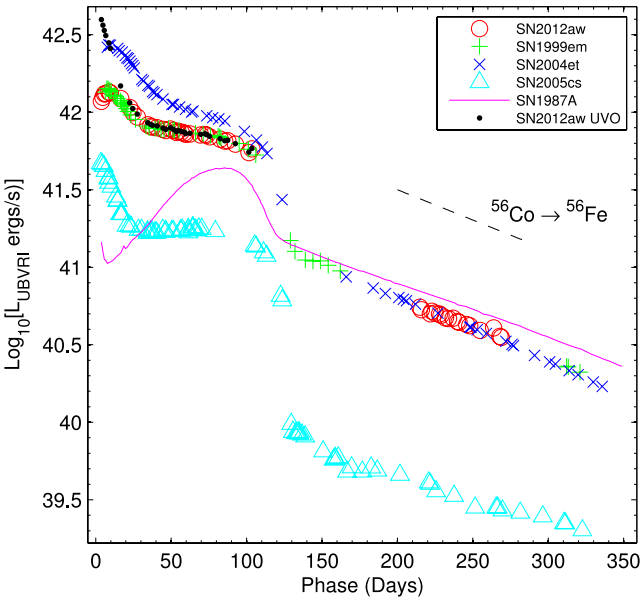

Figure 8. The *UBVRI* bolometric light curve of SN 2012aw is compared with other well-studied SNe. The adopted distances, reddening and time of explosion are same as in Fig. 5. The exponential decline of the radioactive decay law is shown with dashed lines.

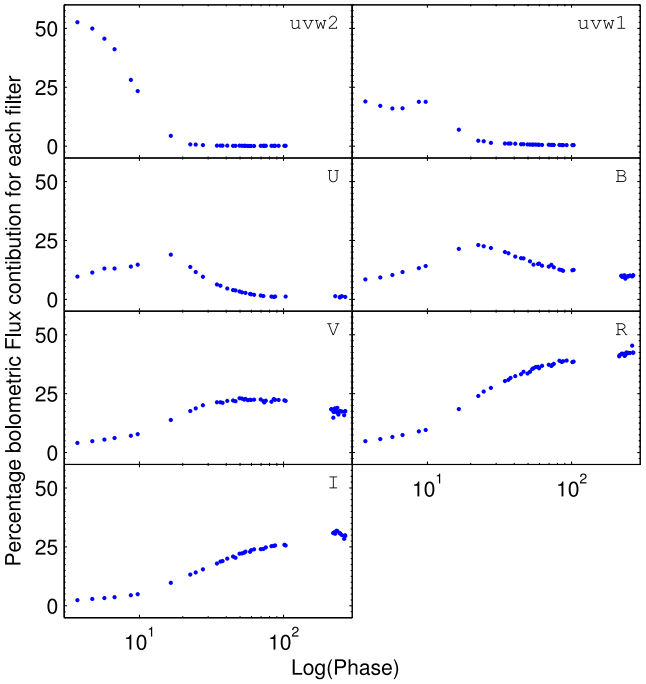

Figure 9. The percentage flux contribution in different passbands in the UVOT $uvw2$, $uvw1$ and optical *UBVRI*. Fluxes are corrected for extinction.

hotter, the major contribution (∼80 per cent) to the bolometric light comes from the UV and *UB* bands, while at later phases the flux contribution from *RI* and near-infrared (IR) bands dominates (Misra et al. 2007). Here, we determine pseudo-bolometric light curve by integrating a spline fitted on the *UBVRI* fluxes derived at their respective effective wavelengths using zero-points from Fukugita, Shimasaku & Ichikawa (1995). Fluxes are integrated over wavelength range from 3335 to 8750 Å; the lower and upper bounds are extended to the half-width half-maximum (HWHM) of *U* and *I* bands. Wherever, the observations in a bandpass were missing, the magnitudes were obtained by interpolating the light curves using low-order cubic spline. In order to remove the effect of overlapping wavelengths in the *UBVRI* passbands on the determination of SED from observed fluxes, we equated the known splines convolved with the filter response with that of the observed fluxes. As a guess, we provide initial SED as the spline fitted on observed fluxes and iteratively we construct the true spline SED (whose filter-convolved fluxes match with observed fluxes). In Fig. 8, we plot the bolometric light curve of SN 2012aw and in the same figure we also show the bolometric light derived using UVOT fluxes in $ubw2$ and $uvw1$ bands taken from Bayless et al. (2013). The $uvm2$ flux is not used due to less number of measurements and large uncertainties in magnitudes. To ensure proper comparison, we have applied same scheme to compute bolometric light curve in *UBVRI* bands for other well-studied Type II SNe 1987A (Hamuy & Suntzeff 1990), 1999em (Leonard et al. 2002a), 2004et (Sahu et al. 2006) and 2005cs (Pastorello et al. 2009). Similar to colour curve, the evolution of bolometric luminosity is also similar to SN 1999em. The bolometric luminosity declines rapidly by 0.5 dex in first 30 d of evolution, and then it slowly declines by 0.2 dex by 104 d.

In Fig. 9, we plot the percentage flux contribution in reference to the total bolometric light in the UV–optical region (0.17 to 0.88 μm) from the different passbands. The contribution due to UVOT bands and the optical *UB* shows a sudden change at around 20 d. In $uvw2$, the contribution falls from approximately 50 to 0 per cent; in $uvw1$, it drops to 0 per cent from a level of 25 per cent; while in *U* and *B*, it rises from 10 per cent at 4 d to 22 per cent at about 20 d and falls slowly thereafter to a few per cent level in the plateau and nebular phases. In *V*, *R* and *I* bands, the trend in flux contribution behaves in a similar fashion and it slowly rises from a few per cent at 7 d to above 25 per cent in the plateau phases and beyond. The bolometric luminosity at 25 d and beyond is mainly contributed by the *VRI* bands.

4.4 Mass of nickel

In Type IIP SNe, the radioactive ^{56}Ni is synthesized by explosive burning of Si and O during shock breakout phase of the explosion (Arnett 1980) and hence the nebular phase light curve is mainly powered by radioactive decay of ^{56}Ni to ^{56}Co with half-lifetime of 6.1 d and ^{56}Co to ^{56}Fe with *e*-folding time of 111.26 d emitting energetic γ-rays and positrons. The nebular phase luminosity is assumed to be directly proportional to mass of ^{56}Ni. For a nearby Type II-pec SN 1987A, the mass of ^{56}Ni ($M_{\rm Ni}$) has been determined fairly accurate to be $0.075 \pm 0.005\,{\rm M}_{\odot}$ (Arnett 1996), and hence by assuming similar γ-ray energy deposition and by comparing the bolometric luminosity of SN 1987A at comparable epochs, we can estimate $M_{\rm Ni}$ of SN 2012aw . We note that for comparison, we use *UBVRI* bolometric luminosity of 1987A computed in this work (Section 4.3) instead of already available accurately calculated UV–optical–IR luminosity. For SN 2012aw, the *UBVRI* bolometric luminosity at 240 d is estimated using a linear fit over 18 epochs between 210 and 270 d, which is $4.53 \pm 0.11 \times 10^{40}$ erg s^{-1}. Similarly for 1987A, it is estimated to be $5.82 \pm 0.06 \times 10^{40}$ erg s^{-1}. The ratio of SN 2012aw to 1987A is found to be 0.778 ± 0.021 and

hence we calculate the value of $M_{\rm Ni}$ for SN 2012aw to be $0.058 \pm 0.002\,{\rm M}_{\odot}$.[3]

The value of $M_{\rm Ni}$ can be independently estimated using the tail luminosity ($L_{\rm t}$) as described by Hamuy (2003), assuming that the γ-rays emitted during radioactive decay of ^{56}Co make the ejecta thermalized viz.

$$M_{\rm Ni} = 7.866 \times 10^{-44} \times L_{\rm t} \exp\left[\frac{(t_{\rm t} - t_0)/(1+z) - 6.1}{111.26}\right] {\rm M}_{\odot},$$

where t_0 is the explosion time, 6.1 d is the half-lifetime of ^{56}Ni and 111.26 d is the e-folding time of the ^{56}Co decay emitting energy in the form of γ-rays. We compute $L_{\rm t}$ at 11 epochs between 215 and 265 d using the observed V magnitude, a bolometric correction of 0.26 ± 0.06 mag during nebular phase (Hamuy 2003), and the adopted reddening and distance (see Table 1). The weighted mean of $L_{\rm t}$ is $8.97 \pm 0.19 \times 10^{40}$ erg s^{-1}corresponding to mean phase of 240.35 d, and this results in a value of $M_{\rm Ni} = 0.057 \pm 0.012\,{\rm M}_{\odot}$. Taking weighted average of the values derived above using two photometric methods, we adopt value of $M_{\rm Ni}$ as $0.058 \pm 0.002\,{\rm M}_{\odot}$ for SN 2012aw.

We note that the value of $M_{\rm Ni}$ estimated for Type IIP SNe using bolometric luminosity of nebular phase depends considerably on the adopted distance and extinction. For example, the value of $M_{\rm Ni}$ reported in the literature (Takáts & Vinkó 2012, see their table 1, hereafter TV12) for SNe 2005cs, 1999em and 2004et varies from 0.003 to $0.008\,{\rm M}_{\odot}$, from 0.022 to $0.036\,{\rm M}_{\odot}$, and from 0.056 to $0.068\,{\rm M}_{\odot}$, respectively. However, in view of the empirical correlation found between the mass of ^{56}Ni and the mid-plateau photospheric velocity by Hamuy (2003) using a large sample of type IIP SNe, the observed object-to-object variation in mass of ^{56}Ni for the above three cases appears to be realistic as the mid-plateau ($\sim$50 d post-explosion) photospheric velocity of SNe 2005cs, 1999em and 2004et estimated using the SYNOW modelling of spectra is found to be 1200, 3400 and 3750 km s^{-1}, respectively (TV12). Considering the uncertainty in the adopted distance and extinction for SN 2012aw we anticipate that it produced the amount of ^{56}Ni equal to or a bit less than that for SN 2004et and this is further corroborated by the fact that the mid-plateau photospheric velocity of SN 2012aw is found to be higher than that of SN 1999em but similar to SN 2004et at comparable epochs (Section 5.4).

5 OPTICAL SPECTRA

5.1 Key spectral features

The spectroscopic evolution of SN 2012aw is presented in Fig. 10, in which a preliminary identification of spectral features is done as per the previously published lines for type IIP events by Leonard et al. (2002a) and the absorption component of some prominent lines is marked. All the spectra are corrected for recession velocity of the host galaxy (Section 2.2). The early phase (7 and 8 d) spectra can be distinguished with the featureless blue continuum having broad P-Cygni profiles of hydrogen H I (Hα 6562.85 Å, Hβ 4861.36 Å, Hγ 4340.49 Å, Hδ 4101.77 Å) and helium He I 5876 Å. The He I line disappears by $\sim$16 d as the continuum becomes redder with time corresponding to a sudden drop in $T_{\rm bb}$ by a factor of 2 to 7 kK since early phase. The appearance of He I line since early phases and its disappearance exactly at $\sim$16 d is also seen in SN 1999em (Leonard et al. 2002a). The Balmer lines of H I are seen at all the phases until 270 d. The FWHM of the emission component of Hα decreases from $\sim$17000 km s^{-1} at 7 d to about 2500 km s^{-1} at 270 d, indicating a decrease in temperature and opacity of the H I line-emitting regions.

In addition to the regular features of H I and He I, the early (7 and 8 d) spectra have a couple of peculiar absorption features. Two weak absorption features are present at $\sim$4300 and $\sim$4850 Å while two relatively strong absorption features are seen near $\sim$5500 Å (marked with A) and near 4500 Å (marked with B). Similar features have also been identified in the early spectrum of Type IIP SNe 1999em (Leonard et al. 2002a), 1999gi (Leonard et al. 2002b) and 2007od (Inserra et al. 2011). The origin of these features is not completely understood and in most of the cases they are explained as high-velocity (HV) component of H I and He I lines; however, the presence of N II lines 4623 Å 5029 Å and 5679 Å have also been explored and these lines cannot be completely ruled out (Baron et al. 2000; Inserra, Baron & Turatto 2012a).

In SN 2012aw, the feature A at 7 d is at $\sim$17665 km s^{-1} with reference to He I rest wavelength, thus making it $\sim$7198 km s^{-1} higher than the existing He I absorption feature velocity. This component decreases to $\sim$16643 km s^{-1} at 8 d making an offset by $\sim$6586 km s^{-1} higher than existing He I feature. Another absorption feature B is also located at a velocity position of $\sim$21785 km s^{-1} on 7 d in reference to rest Hβ making it higher by $\sim$11293 km s^{-1} over the existing Hβ absorption trough. This feature decreases to $\sim$21477 km s^{-1} on 8 d. Both of these features tend to decrease in velocity with time, however, none of these features could be detected on 12 d and after. The HV absorption features are not seen in Hα. In Fig. 11, we compare the early phase spectra with other SNe and it can be seen that such HV features indicating existence of very HV line-forming material have also been observed for SN 1999gi (Leonard et al. 2002b) and SN 1999em (Baron et al. 2000; Leonard et al. 2002a). In the day 1 spectra of SN 1999gi, the HV component was more dominant and it appeared at $-30\,000$ km s^{-1} with no trace of normal absorption components. Inserra et al. (2012a) detect HV absorption to Hβ and Hγ lines only in a bright ($M_V = -18$) Type IIP SN 2007od, and a detailed spectral analysis using PHONEIX favoured the presence of HV feature. It appears that such HV features in Hβ and He I are ubiquitous in normal luminosity Type IIP SNe at early phases ($\leq$8 d) though their origin (i.e. whether it is caused by abundance and/or density enhancements in the layers of ejecta above photosphere) and exact geometry remain open questions to be addressed using detailed modelling. We attempt to identify these peculiar absorption features using the SYNOW modelling in Section 5.2.

The spectra at 12, 15 and 16 d represent transition from a hotter ($\sim$16kK) early phase to a cooler ($\sim$6kK) plateau phase when the photosphere begins to penetrate Fe-rich ejecta. These spectra mark the emergence of permitted lines of singly ionized atoms of calcium, iron, scandium, barium, titanium and of neutral sodium atoms. The strong lines of Ba II 4554 Å blend and Fe II 5169 Å begin to appear at 12 d, and the weaker lines of Fe II at 4929 and 5018 Å are clearly seen at 20 d. The spectra at eight epochs from 20 to 104 d represent the plateau phase corresponding to further slow cooling of the SN envelope and appearance of more number of metallic lines. The lines of Na I D 5893 Å and Ca II IR triplet 8498, 8542, 8662 Å emerge at 20 d and they are clearly visible by 31 d. The blend of Ca II H 3934 Å and K 3968 Å appear at the gf-weighted rest wavelength 3945 Å and it is very strong at 20 d, and seen until 104 d. A definite identification of Ca II is seen in the early spectrum of IIP SNe as well, e.g. at 12 d

[3] Using the same method and adopting the distance and extinction as given in Fig. 5, we estimate $M_{\rm Ni}$ for comparison: SNe 2005cs, 1999em and 2004et as 0.004 ± 0.001, 0.053 ± 0.001 and $0.058 \pm 0.001\,{\rm M}_{\odot}$, respectively.

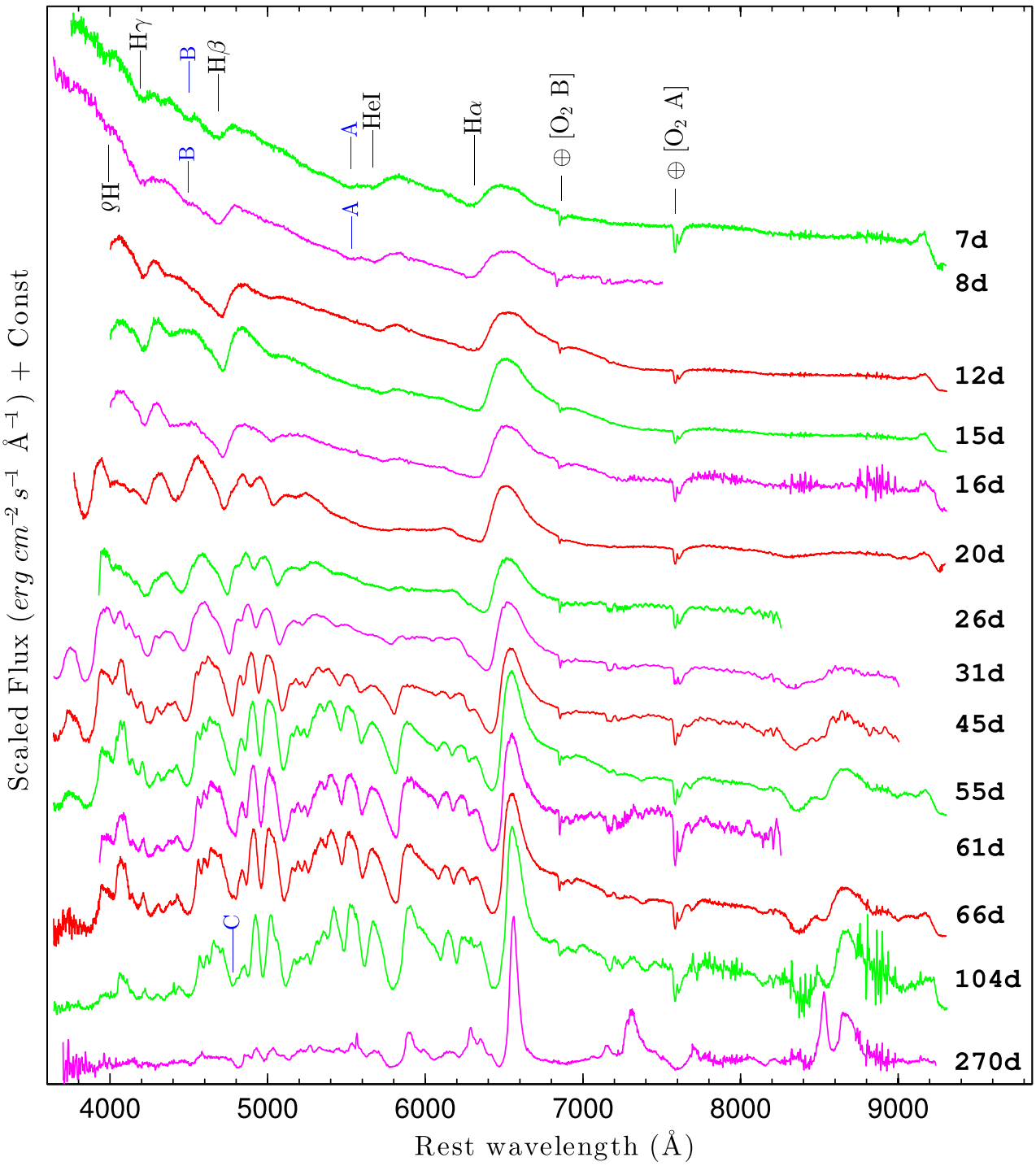

Figure 10. The Doppler corrected spectra of SN 2012aw are shown for 14 phases during 7 to 270 d. The prominent P-Cygni profiles of hydrogen (Hα, Hβ, Hγ, Hδ) and helium (He I 5876 Å) lines are marked. The peculiar absorption features marked with A, B and C are discussed in the text. The telluric absorption features are marked with $\oplus$ symbol. The portions of spectrum at extreme blue and red end have poor SNR.

in SN 1999em (Baron et al. 2000). The Fe II 5535 Å blend, Sc II 5665 Å multiplet, Ba II 6142 Å and Sc II 6246 Å are clearly seen at 45 d. The above features are present in the spectra until 104 d and their comparison with other SNe (Fig. 11) indicates that the plateau phase spectral features are similar to normal type IIP events.

The only late time spectrum at 270 d shows emission lines with no absorption components, which is a typical characteristic feature of nebular phase spectra of IIP SNe. A comparison of the 270 d spectrum is made with other SNe in Fig. 11 and a preliminary identification of nebular lines is shown in Fig. 12. The forbidden emission lines of [O I] 6300, 6364 Å, [Ca II] 7291, 7324 Å and [Fe II] 7155, 7172 Å; permitted emission lines of H I, Na I 5893 Å doublet and Ca II 8600 Å triplet become the dominant spectral features.

The presence and evolution of spectral features of SN 2012aw during the early, plateau and nebular phases show striking similarity with other well-studied normal Type IIP SNe 1999em

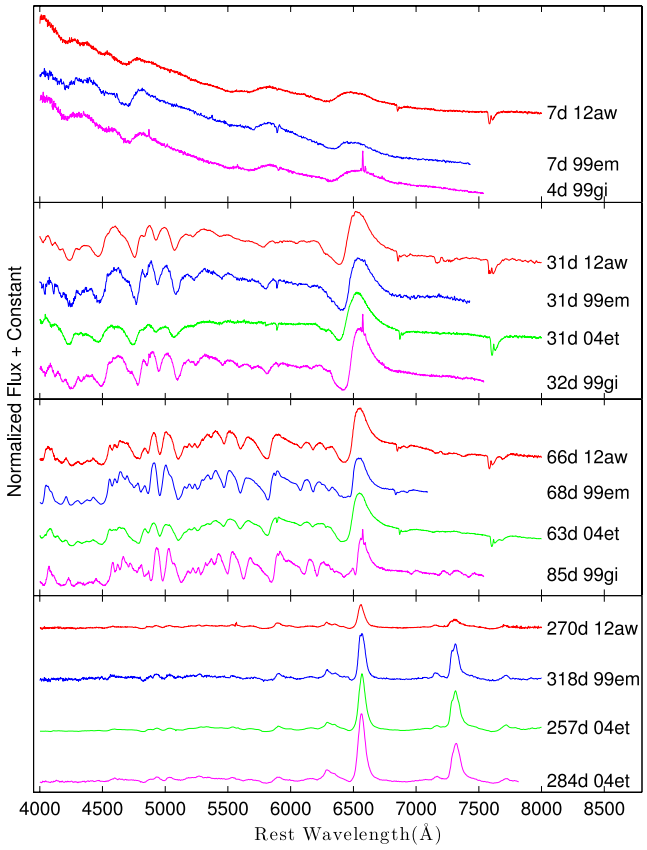

Figure 11. Comparison of the early (7 d), plateau (31, 66 d) and nebular (270 d) phase spectra of SN 2012aw with other well-studied Type IIP SNe 1999em (Leonard et al. 2002a), 1999gi (Leonard et al. 2002b), 2004et (Sahu et al. 2006; Maguire et al. 2010). Observed fluxes of all the SNe are corrected for extinction and redshift (adopted values same as in Fig. 5).

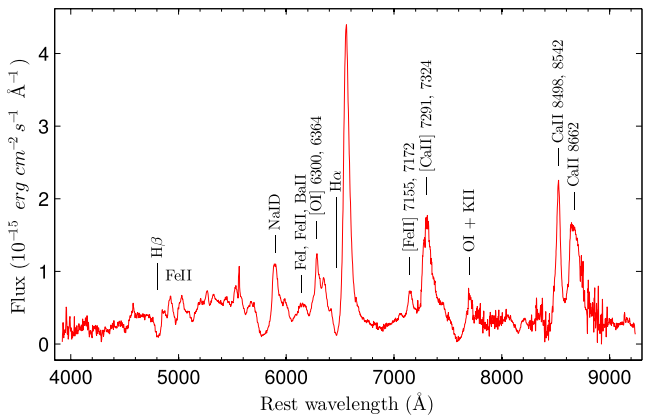

Figure 12. The nebular phase spectrum of SN 2012aw at 270 d.

(Leonard et al. 2002a), 1999gi (Leonard et al. 2002b) and 2004et (Sahu et al. 2006). However, in order to identify and interpret weak spectral features, to estimate the velocities of photospheric/ejecta layers and to understand how the layers of line-forming regions evolve with time and vary among object to object, we perform the SYNOW modelling of the spectra in the next section.

5.2 SYNOW modelling of spectra

We modelled the spectra of SN 2012aw with the parametrized SN spectrum synthesis code SYNOW 2.3[4] (Fisher et al. 1997, 1999; Branch et al. 2002). In contrary to the full non-local thermodynamic equilibrium (NLTE) model codes CMFGEN (Dessart & Hillier 2005b) and PHONEIX (Baron et al. 2004), SYNOW assumes – simple local thermodynamic equilibrium (LTE) model atmospheres having a sharp photosphere emitting a blackbody continuum and a spherically symmetric SN expanding homologously; the line formation is due to pure resonant scattering and radiative transfer is computed by employing the Sobolev approximation. We tried three different options for optical depth profiles (viz. Gaussian, exponential and power law), no significant differences were noticed; however, while matching absorption minimum, the exponential profile, $\tau \propto \exp(-v/v_e)$, where v_e, a profile fitting parameter, e-folding velocity, was found to be the most suitable and is adopted here. One important aspect of the SYNOW model is the detachment of an ion (line-forming layer) from the photosphere which is achieved by setting the minimum velocity of the ion greater than the photospheric velocity resulting in flat-topped emission and blue-shifted absorption counterpart. Strong Hα P-Cygni can be partially fitted in absorption minima with detached H I only, while the strong emission part remains unfitted with a flat-topped crest.

The observed spectra are Doppler-corrected and dereddened, before visually fitting the model SYNOW spectra with the observed ones. We have modelled the spectra for all the 14 phases and the best-fitting values of T_{bb} to match the continuum are given in Table 6. These SYNOW-derived temperatures are consistent with the ones derived photometrically (Section 4.2). In the early phase spectra, the continuum is fitted properly as it agrees well with the SYNOW's approximation of LTE atmosphere, whereas at later phases, the continuum is quite deviant, though we are able to match the spectral lines. In Fig. 13, we show the modelled spectra at 7, 31 and 61 d including the common set of contributing species (H I, He I, etc.) and an additional set of species N II, Fe II, Ti II, Sc II, Ca II, Ba II, Na I, Si II, O I and N I, respectively. It can be seen that the model spectra are able to match and reproduce most of the features present in the observed spectra. The optimization of v_{ph} is done to match the absorption minima of Fe II multiplet (4924, 5018, 5169 Å) during the plateau phase and of He I 5876 Å line during early phase spectra.

The 7 d spectrum shows a well-matched continuum with P-Cygni profiles of Hα, Hβ, Hγ, Hδ and He I. The suspected absorption due to the HV component of Hβ and He I is explored further by introducing nitrogen, and the SYNOW modelling appears to be consistent with the absorption dips near 4512, 4834 and 5528 Å, which correspond to N II lines of rest wavelength 4623, 5029 and 5679 Å, respectively. The N II lines of 4623 and 5679 Å are also seen in the 8 d spectrum (Fig. 11) and they disappear thereafter. Using full-NLTE modelling with PHONEIX of the 7 d spectrum of SN 1999em, Barbon et al. (1990) have reproduced absorption features using N II lines indicating the presence of enhanced nitrogen and helium. We conclude that early time spectral features of SN 2012aw were much similar to normal IIP SNe 1999em as well as 1999gi. We, however, note that in the 5 d spectrum of bright Type IIP SN 2007od, the presence of absorption dips near 4500 and 4800 Å and the absence of absorption dips near 5500 Å favoured the presence of HV components (Inserra et al. 2012a). The He I feature in SN 2012aw disappears at ∼16 d and a prominent Na I D feature begin to emerge

[4] http://www.nhn.ou.edu/~parrent/synow.html

Table 6. The best-fitting blackbody continuum temperature (T_{bb}) and the line velocities of Hα, Hβ, Fe II (4924 Å, 5018 Å, 5169 Å) and He I 5876 Å as estimated from the SYNOW modelling of the observed spectra of SN 2012aw. Velocities derived using lines of Fe II or He I are taken to represent the velocity of the photosphere (v_{phm}).

UT date (yyyy-mm-dd)	Phase[a] (d)	T_{bb}[b] (kK)	v(He I) 10^3 km s^{-1}	v(Fe II) 10^3 km s^{-1}	v(H$_\alpha$) 10^3 km s^{-1}	v(H$_\beta$) 10^3 km s^{-1}
2012-03-22	7	16.5	11.2	–	12.8	11.2
2012-03-23	8	15.5	10.7	–	12.8	11.0
2012-03-27	12	14.0	9.0	–	11.7	9.7
2012-03-30	15	13.5	8.65	–	10.6	9.3
2012-03-31	16	12.5	8.5	8.6	10.4	9.2
2012-04-04	20	10.5	–	7.7	10.0	8.6
2012-04-10	26	7.5	–	6.55	8.8	7.3
2012-04-15	31	7.5	–	5.6	7.9	6.6
2012-04-29	45	5.5	–	4.5	6.4	5.2
2012-05-09	55	5.2	–	4.15	5.5	4.8
2012-05-15	61	5.2	–	3.5	5.0	4.2
2012-05-09	66	5.2	–	3.5	5.0	4.2
2012-06-27	104	4.9	–	2.9	3.8	3.0
2012-12-10	270	3.9	–	1.6	3.4	1.6

[a]With reference to the time of explosion JD 245 46002.59.
[b]Best-fitting blackbody temperature of photosphere to match the continuum in the observed spectrum.

from 26 d at similar location. In the plateau phase spectra, we have also incorporated ions Fe II, Sc II, Si II, Ca II and heavy ions Ti II, Ba II of which most are present as blended or weaker features in the spectra.

The lines of Si II at 6347 Å and 6371 Å appearing as a blend at 6355 Å can be seen in the bluer wing of broad P-Cygni Hα absorption, which start to appear at about 26 d when T_{bb} drops down to about 7500 K and it can been seen until 104 d (Figs 10, 13 and 14). This feature is also seen in the spectra of SN 1999em at similar phases, though it has been identified as a HV component of Hα (Leonard et al. 2002a). In SN 2012aw this feature is fitted well with Si II 6355 Å blend in 31 and 61 d spectra for the photospheric velocity at respective phases and hence we rule out the possibility of this being a HV component. We note that the Si II feature is also identified in the hotter early time (<10 d) spectra of SN 1999em, which we do not see in SN 2012aw.

The feature marked with C in Fig. 10 is analysed further using the SYNOW modelling. We find that it is most probably a HV component of Hβ blended with Ba II and Ti II lines. By a careful inspection of model fits in Fig. 14, it can be seen that this feature actually starts to appear much earlier than 104 d. At 55 d, a very faint impression of this feature appears which does not fit with the SYNOW model feature of Hβ and continues to become increasingly stronger until our last plateau phase spectra at 104 d. At 104 d (modelled with Hβ regular and HV component blend) this feature became strong enough to suppress the existing regular Hβ feature and appears as an entire separate absorption component. By SYNOW modelling the 104 d spectra, none of the independent atomic species and single Hβ component could be accounted for this feature. Only a HV Hβ component of ∼5200 km s^{-1} along with blend of Ba II and Ti II lines could match the feature, whereas the regular Hβ component remains in line with the existing velocity trend at a velocity of ∼3000 km s^{-1} only. Similar problem was also encountered with 104 d Hα feature which is not much apparent by eye inspection, but single Hα component in model spectra was unable to fit the broadened Hα absorption dip in the observed spectra. Although no separate absorption dip was seen here, but the absorption feature of Hα is somewhat broadened which, only a blend of HV component along with regular Hα, can fit. This HV component is found to be at ∼5800 km s^{-1} whereas the regular Hα component is at ∼3800 km s^{-1} which falls in line with the existing Hα velocity evolution. It is also to be noted that velocity difference of HV component with the regular component is ∼2000 km s^{-1} for both Hα and Hβ, which might indicate that the origin of both HV components is from a single H layer whose velocity is ∼2000 km s^{-1} higher than the actual layer responsible for the photospheric velocity. A careful examination of Hβ profiles in Fig. 11 at phase 60 d indicate that the feature similar to C is absent in the spectra of SNe 1999em and 1999gi; however, this feature is present in spectrum of SN 2004et. The presence of HV components of Hα and Hβ have been observed throughout the photospheric phase until 105 d in a bright ($M_V = -17.67$) Type IIP SN 2009bw (Inserra et al. 2012b) suggestive of interaction between the SN ejecta and the pre-existent CSM. We, therefore, suggest that the broadening of Hβ and possibly Hα during 55 to 104 d indicate ejecta–CSM interaction in SN 2012aw.

The presence of absorption feature due to O I line at 7774 Å is clearly reproduced by SYNOW in the 61 d spectrum. The O I line begin to appear at 31 d and it is clearly seen until 104 d. The N I 8130 Å line is marginally detected as its identification is affected by the poor SNR. The absorption features seen ∼9000 Å in 55 and 66 d spectra (see Fig. 10) are most likely due to C I 9061 Å. The appearance of absorption features in the plateau phase spectra due to O I and occasionally also due to C I and N I have also been observed in normal Type IIP SN 1999em (Leonard et al. 2002a), bright IIP SN 2009bw (Inserra et al. 2012b), subluminous IIP SNe 2009md (Fraser et al. 2011), 2005cs (Pastorello et al. 2009) and 2008in (Roy et al. 2011). Several weak absorption features viz. Fe II 4629 Å, Sc II 4670 Å, Fe II 5276 Å and Fe II 5318 Å are identified.

5.3 Evolution of spectral lines

The evolution of spectral features provide important clues about the interaction of expanding ejecta with the CSM, formation of dust in the ejecta and geometrical distribution of ejecta. To illustrate the

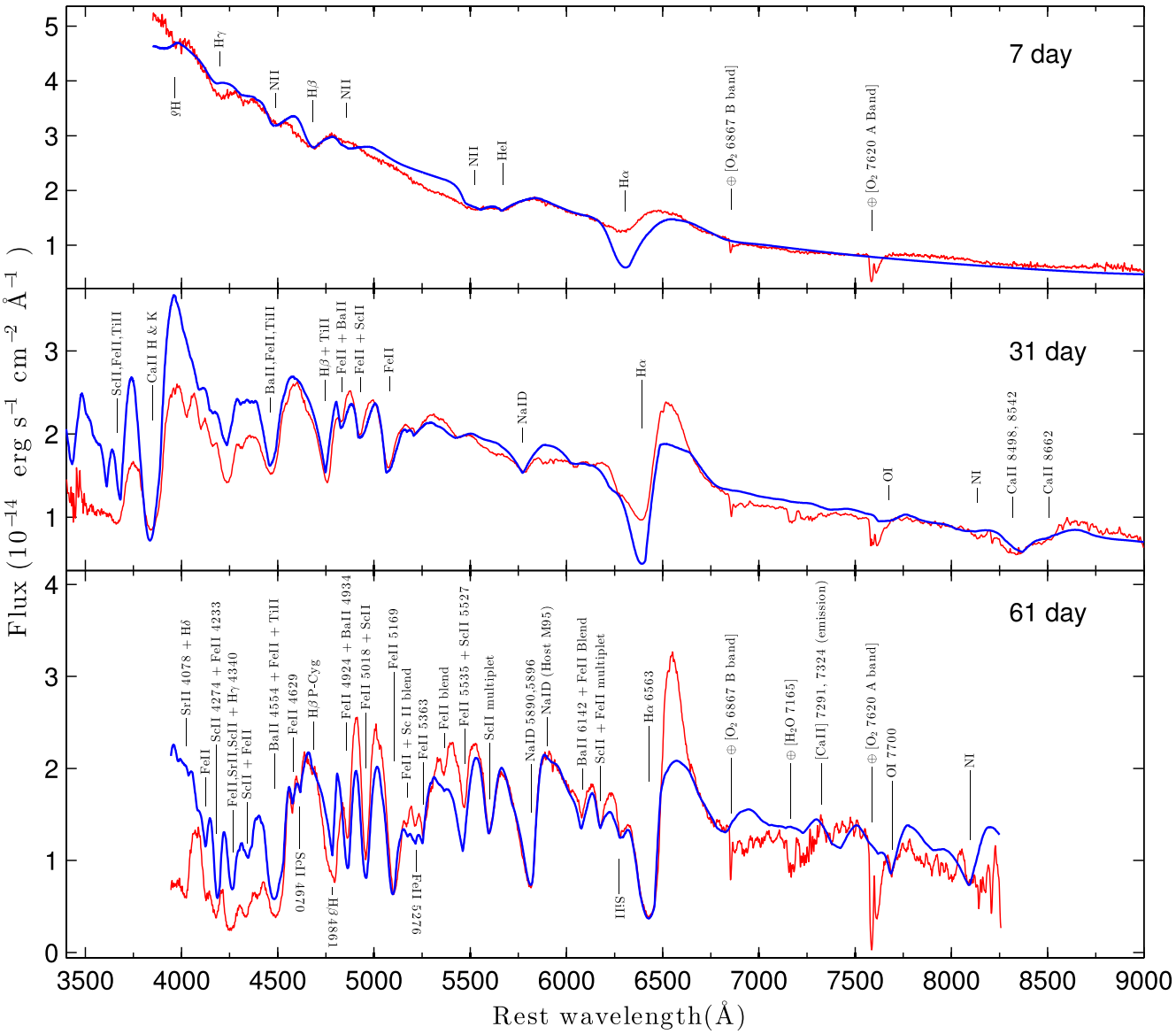

Figure 13. The SYNOW modelling of 7, 31 and 61 d spectra of SN 2012aw. Model spectra are shown with thick solid line (blue), while the observed ones are in thin solid line (red). Observed fluxes are corrected for extinction.

evolution of individual lines, a portion of spectrum is plotted in Fig. 15 from 7 to 207 d in velocity domain corresponding to rest wavelengths of Hβ 4861 Å, Na I D 5893 Å, Ba II 6142 Å and Hα 6563 Å. Broad Hα P-Cygni (FWHM $\sim$ 17000 km s^{-1}) is prominent from as early as first epoch 7 d spectra and is present all throughout which evolves into narrow feature (FWHM $\sim$ 2500 km s^{-1}at 270 d) with time. Apart from blue-shifted absorption trough of the P-Cygni, which is the indicator of expansion velocity, the emission peak is also blue shifted by 4500 km s^{-1} at 7 d (2700 km s^{-1}at 15 d, 2100 km s^{-1} at 31 d), it almost disappears by 66 d (600 km s^{-1}) and settles to rest in the late plateau spectrum of 104 d (300 km s^{-1}). The blueshift of emission peak in early time (plateau) spectra is also seen in Hβ and such features are similar with those observed in other type II SNe namely SNe 1999em (Elmhamdi et al. 2003), 2004et (Sahu et al. 2006) and 1987A (Hanuschik & Dachs 1987) and it has been theoretically explained as being due to scattering of the photons from the receding part of the ejecta (Chugai 1988; Jeffery & Branch 1990).

A comparison of nebular phase 270 d Hα line profile with other SNe (Figs 11 and 16) indicate that the Hα line flux was lower than that of SNe 1999em and much lower than 2004et. Whereas the FHWM of Hα appears to be similar (i.e. $\sim$2600 km s^{-1}) for these three SNe, suggesting that the expansion velocity of line-emitting region has been quite similar. Moreover, Hα appears to be quite symmetric around zero velocity indicating a spherically symmetric distribution of hydrogen envelope. This is in contrary to that observed for SN 2006bp, whose profile is highly asymmetric suggesting that explosion has been quite asymmetric or the dust is forming. The blueshift in Hα emission peak can also result from preferential attenuation of red wings due to formation of dust in the ejecta. The indication of dust formation is seen in SN 1999em after 500 d (Elmhamdi et al. 2003) and in SN 2004et after 320 d (Sahu et al. 2006; Maguire et al. 2010). The presence of blueshift ($\sim$1500 km s^{-1}) in Hα emission peak has been seen from 226 to 452 d spectra of IIP SN 2007od (Inserra et al. 2012b) and this has been explained by the presence of dust in the

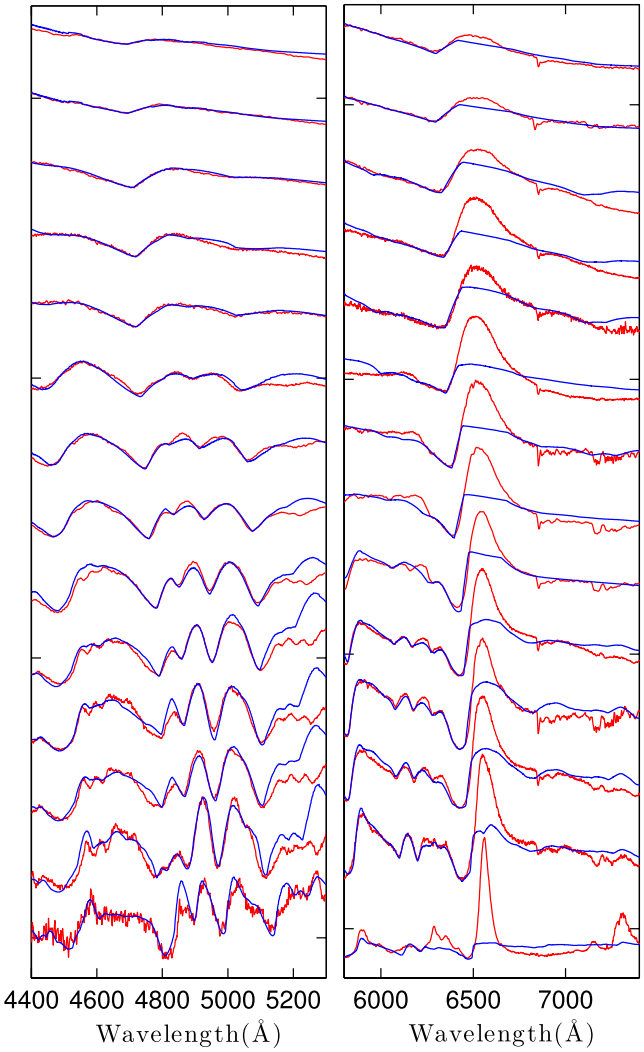

Figure 14. The SYNOW modelling (blue) for Fe II multiplet (left) and Hα (right) profiles over the observed spectra (red) are shown. The spectral evolution is shown from top to bottom at 14 phases from 7 to 270 d. Detached H is used to fit the absorption dip. In addition to Fe II and H I; other ions (Sc II, Ba II, Si II and Na I, Ti II are also incorporated in model to fit some weaker features, specially at later phases. The phases of plotted spectra are 7, 8, 12, 15, 16, 20, 26, 31, 45, 55, 61, 66, 104 and 270 d (top to bottom).

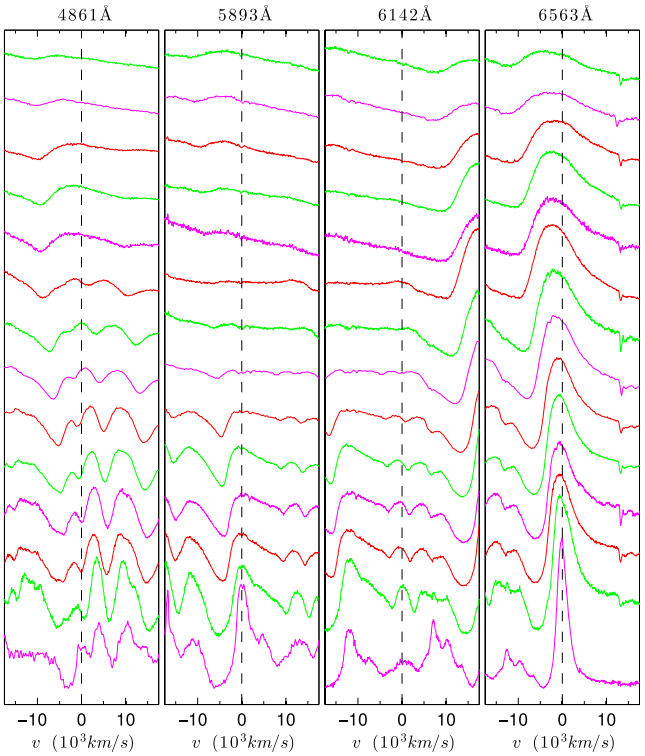

Figure 15. Evolution of line profiles for Hβ, Na I D, Ba II and Hα are plotted at 14 phases from 7 to 270 d top to bottom. The zero-velocity line is plotted with dotted line and the corresponding rest wavelength is written on top. The phases of plotted spectra are 7, 8, 12, 15, 16, 20, 26, 31, 45, 55, 61, 66, 104 and 270 d (top to bottom).

ejecta. We note that observational signatures related to early dust formation and the ejecta–CSM interaction for SN 2012aw are unlike that of bright ($M_V \sim -18$ mag) IIP SNe 2007od, 2009bw and 2006bp.

The He I 5876 Å is prominent from early 7 d spectra which disappear rapidly and can be traced only up to 16 d. Several metal features start to appear from 26 d. The Si II 6355 Å feature is found to appear on the blue wing of Hα at $\sim -12\,000$ km s^{-1} and evolved monotonically until the last plateau phase spectra at 104 d. The Na I D doublet 5890, 5896 Å feature start to appear at position very close to earlier He I feature, and it persists up to nebular phase at 270 d. The location of Na I D emission peak at zero velocity indicates an almost spherical distribution of the Na in the ejecta material. The absorption dips due to *s*-process elements Ba II 6142 Å and Sc II 6248 Å start to appear and strengthen until the last plateau spectra 104 d. The O I lines start to appear at 104 d and it is seen clearly in the 270 d spectrum. Similar to Hα line, the O I line flux is too smaller than that of SNe 1999em and 2004et, though the terminal velocity is of similar order (see Fig. 16).

5.4 Ejecta velocity

The expansion velocity of the photosphere ($v_{\rm ph}$) coupled with the mass of ejected matter ($M_{\rm ej}$) provides strong constraints on the kinetic energy ($E_{\rm kin}$) of explosion. The photosphere represents the optically thick and mostly ionized part of the ejecta which emits most of the continuum radiation as a 'diluted blackbody'. This photosphere is located in a thin spherical shell where electron-scattering optical depth of photons is $\sim^2/_3$ (Dessart & Hillier 2005a). In Type IIP SNe, no single measurable spectral feature is directly connected with the true velocity of the photosphere; however, during the plateau phase, it is best represented by blue-shifted absorption components of P-Cygni profiles of Fe II at 4924, 5018 and 5169 Å, while in early phase the lines of He I 5876 Å or Hβ act as a good proxy (see TV12 for a detailed review on estimating the photospheric velocities of Type IIP SNe). We can estimate velocities either by measuring Doppler-shift of the absorption minima using SPLOT task of IRAF or by modelling the observed spectra with SYNOW. The latter gives better estimate of $v_{\rm ph}$, as it can take care and reproduce line blending; however, for the sake of comparing velocities of SN 2012aw with other SNe in the literature, we use both the methods in this work and the corresponding velocities are denoted as $v_{\rm pha}$ and $v_{\rm phm}$, respectively. Apart from Fe II lines, the expansion velocities of line-forming layers for Hα, Hβ, He I and Sc II are also estimated.

Using SYNOW we obtain the best fit locally, employing the whole wavelength range may lead to over- or underestimate of velocities

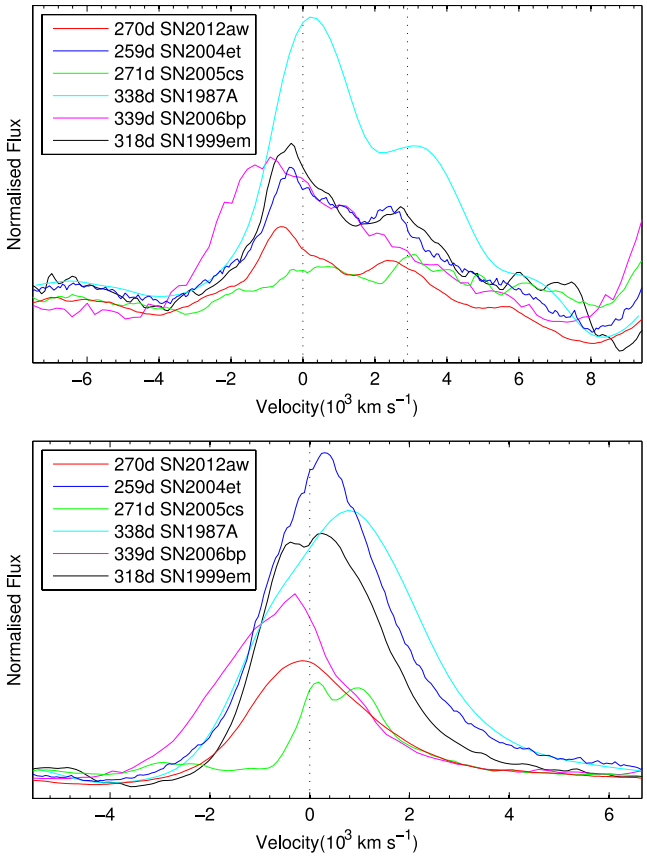

Figure 16. The velocity profiles of O I doublet (left) and Hα are compared with other SNe from the literature. The spectra have been corrected for recession velocities of respective host galaxies. The sources for the spectra are: SN 1987A (Pun et al. 1995), SN 1999em (Leonard et al. 2002a), SN 2004et (Sahu et al. 2006), SN 2005cs (Pastorello et al. 2009) and SN 2006bp(Quimby et al. 2007).

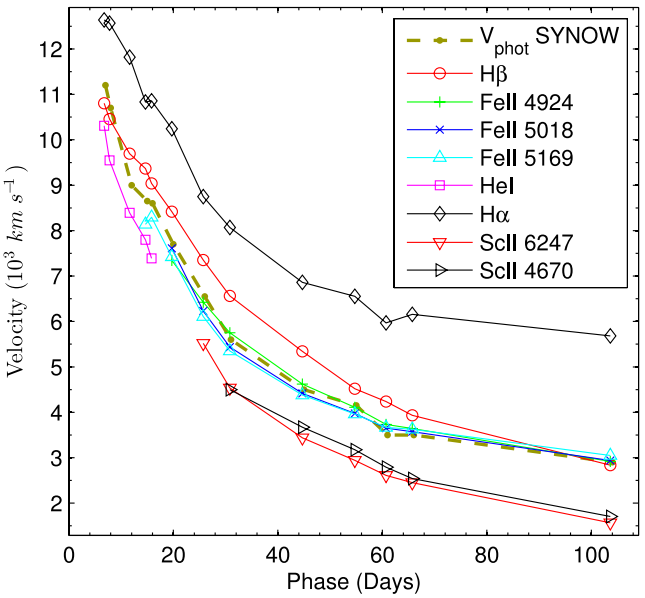

Figure 17. Line velocity evolution of Hα, Hβ, He I, Sc II and Fe II. The velocities are estimated using Doppler-shift of the absorption minima. The expansion velocity of the photosphere ($v_{\rm phm}$) estimated from SYNOW fits of He I line until 15 d and simultaneous fits for Fe II lines at later phases (see Table 6) are overplotted for comparison.

due to formation of lines at different layers. Fig. 14 shows best fitted profiles over ∼1000 Å wide wavelength regions around Hα and Fe II along with Hβ features. It can be seen that the best-fitting model spectra are able to reproduce the absorption components of Hβ , Fe II 4924 Å, Fe II 5018 Å and Fe II 5169 Å simultaneously. At early phases from 7 to 16 d, the best-fitting model velocity for He I 5876 Å line is also estimated. The model-derived velocities are listed in Table 6 and the value of $v_{\rm phm}$ represent He I line until 15 d and Fe II lines at phases thereafter. The typical uncertainty in velocities estimated by deviation seen visually from best-fitting absorption troughs by varying $v_{\rm phm}$ is ∼150 km s^{-1}. This is consistent with the values obtained using automated computational techniques viz. χ^2 minimization and cross-correlation methods (TV12).

The expansion line velocities of Hα, Hβ, He I, Fe II (4924 Å, 5018 Å and 5169 Å) components, Sc II 6246 Å and Sc II 4670 Å blend have also been determined using IRAF by fitting the absorption trough with a Gaussian function and these are shown in Fig. 17. It can be seen that H I (Hα, Hβ) lines formed at larger radii (i.e. higher optical depths) than He I, while the Fe II lines are formed at lower radii. The Sc II lines are formed at even lower optical depths and the velocities derived using Sc II 4670 and 6247 Å at phases 26 d onwards are systematically lower by ∼1000 km s^{-1} from that of Fe II lines or of $v_{\rm phm}$. During 16 to 104 d, it can be seen that velocities derived using individual lines of Fe II are same within errors and these values are further in agreement with those determined using SYNOW (i.e. simultaneous fits to Fe II lines). At early phases (<15 d), the SYNOW-determined values from He I are found to be consistently higher by ∼1000 km s^{-1} from those determined using absorption minima; however, at phases 7 and 8 d these values are consistent with those obtained from Hβ absorption minima. The Hα velocity is higher than $v_{\rm phm}$ by ∼2000 km s^{-1} at early phases and by ∼1000 km s^{-1} at later phases. As noted by TV12, we confirm that the line velocities of Hβ are in agreement with that of $v_{\rm phm}$ above 10 000 km s^{-1} , while below this it is consistently higher than those determined using Fe II lines. The value of $v_{\rm phm}$ falls from 2900 km s^{-1} at 104 d to 1600 km s^{-1} at 270 d.

Fig. 18 shows the comparison of the photospheric velocity of SN 2012aw with other well-studied SNe 1999em, 1999gi, 2004et, 1987A and 2005cs. For this comparison purpose, the absorption trough velocities (average of Fe II lines at late phases and He I at early phases) have been used as the SYNOW-derived velocities are not available for all the SNe considered for comparison.[5] The velocity evolution of SN 2012aw is similar to the normal Type IIP SNe 2004et, 1999em and 1999gi; though it is strikingly different than that of subluminous SN 2005cs and the Type II-peculiar SN 1987A. The velocities of SN 2005cs are extremely less than SN 2012aw at all phases by ∼3000 km s^{-1}, whereas the profile of SN 1987A shows sharp decline in early phases (<15 d) and comparatively slower decline in later phases. The entire photospheric velocity profile of SN 2012aw is identical to 2004et at all phases whereas it is consistently higher than that of SNe 1999em and 1999gi by ∼600 km s^{-1} at all phases. We note that while comparing Sc II 6247 Å absorption velocities of SNe 2004et and 1999em, no difference is seen in velocity evolution (Maguire et al. 2010); however, velocities obtained using the SYNOW model fits to the Fe II lines result in systematical

[5] Barring SN 1999em, taken from Leonard et al. (2002a), the velocities for all other comparison SNe are determined in this work using spectra available at SUSPECT http://suspect.nhn.ou.edu

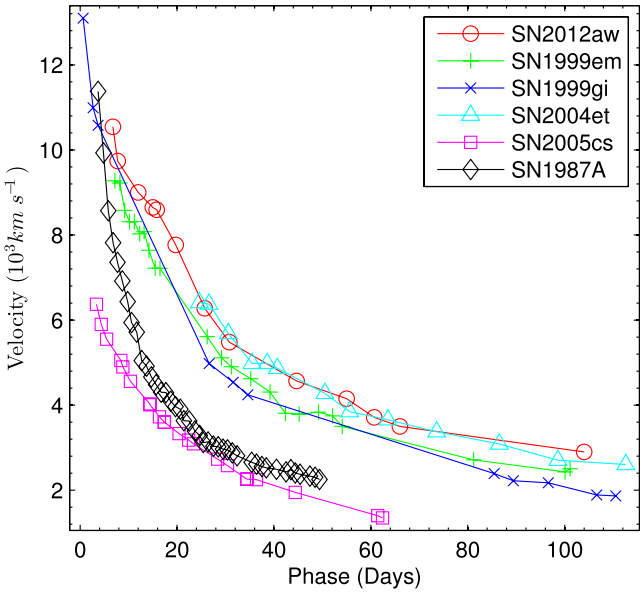

Figure 18. The evolution of the photospheric velocity (v_{ph}) of SN 2012aw is compared with other well-studied SNe. The (v_{ph}) plotted here are the absorption trough velocities (average of Fe II lines at late phases and He I at early phases.

higher velocities for SN 2004et (TV12). Similarly, a comparison of expansion velocities of Hα and Hβ with other SNe indicate that these too are systematically higher than those observed for SNe 1999em and 1999gi, and are comparable with those observed for SN 2004et. For example, at phases 11, 30 and 50 d, respectively, the velocities of Hβ are 11000, 7400 and 5800 km s^{-1} for SN 2004et (TV12); 10000, 6600 and 5000 km s^{-1} for SN 2012aw (Table 6); 8400, 5200 and 3500 km s^{-1} for SN 1999em (TV12).

6 CHARACTERISTICS OF EXPLOSION

6.1 Explosion energy

The radiation-hydrodynamics simulations provided by Dessart, Livne & Waldman (2010) for core-collapse SNe, generated artificially by driving a piston at the base of the envelope of a rotating and non-rotating red-supergiant progenitor stars, suggest that the v_{ph} at 15 d after shock breakout is a good and simple indicator of the explosion energy (E_0), no matter what the initial mass is. For non-rotating solar metallicity models with progenitor masses 11–30 M$_\odot$, a simulated plot of $v_{ph,\,15\,d}$ and the velocity at the outer edge of the oxygen-rich shell $v_{ej,\,O}$ (see fig.4 in their paper) for different energy of explosion ranging from 0.1 to 3 foe (1 foe = 10^{51} erg), indicate that for SN 2012aw corresponding to the value of $v_{ph,\,15\,d}$ = 8650 km s^{-1} (see Table 6), the value of E_0 lies in the range 1 to 2 foe. The value of $v_{ph,\,15\,d}$ for SN 1999em is 7650 km s^{-1} whereas for SN 2004et it is 8800 km s^{-1} (TV12) and hence assuming similar nature of progenitor star, the strength of explosion for SN 2012aw should have been similar to SN 2004et but higher than that of SN 1999em. We note that detailed radiation-hydrodynamic simulations of bolometric light curves obtain value of E_0 of 1.3 ± 0.3 foe for SN 1999em (Utrobin 2007) and of 2.3 ± 0.3 foe for SN 2004et (Utrobin & Chugai 2009).

Furthermore, the simulated models by Dessart et al. (2010), when combined with the width of observed nebular phase O I 6300–6364 Å line, can also be used to place an upper limit of the progenitor main-sequence mass. In nebular phase spectra, an assessment of $v_{ej,\,O}$ can be made by measuring HWHM of O I feature and for SN 2012aw it is found to be ∼1340 km s^{-1} at 270 d and for comparison SNe 2004et, 1999em, 1987A, it is ∼1300 ∼1200 and ∼1400 km s^{-1}, respectively (see Fig. 16). Hence, the simulations for non-rotating models suggest an upper mass of 15 M$_\odot$ for the progenitor star of SN 2012aw. Rotating models suggest lower mass star. This upper mass limit for SN 2012aw is consistent with that determined by Kochanek et al. (2012) using data on pre-SN stars and the stellar evolutionary models. We however note that the simulations of Dessart et al. (2010) assume no mixing of ejecta whereas the study of velocity distribution in line profile shapes of nebular lines by Maguire et al. (2012) indicate that mixing in ejecta is likely to have occurred in Type IIP SNe. Consequently, the width of [O I] lines may not represent true velocity of the oxygen-rich zones and hence the simulations-derived progenitor mass may be regarded as first hand estimates.

6.2 Mass of progenitor star

The mass of progenitor star can be estimated using nebular phase emission line of O I 6300, 6364 Å doublet as a detailed nucleosynthesis yields of the stellar evolution/explosion models indicate that the core mass of metals in the inner ejecta is found to scale with the zero-age main-sequence mass of the progenitor (Woosley & Weaver 1995). Additionally, we also consider that in type II SNe, the nucleosynthesis yield is largely unaffected by late-time evolution of SN ejecta. The mass of oxygen in type II SNe can be estimated by analysis of emission from the nebular phase [O I] doublet which is mainly powered by the γ-ray depositions and more than half of the [O I] doublet luminosity during nebular phase is contributed by the newly synthesized oxygen in the ejecta (Jerkstrand et al. 2012). Also, considering the fact that the SNe 2004et and 1987A have similar ejecta velocities and ^{56}Ni masses, and the mass of oxygen for SNe 2004et and 1987A is modelled quite accurately and is available for comparison. We however note that the comparison with SN 2004et is more relevant as it is spectroscopically and photometrically similar to SN 2012aw. Following Elmhamdi et al. (2003), the luminosity of [O I] doublet can be written as

$$L_{6300} = \eta \frac{M_O}{M_{ex}} L(^{56}\mathrm{Co}),$$

where M_O is the mass of oxygen, M_{ex} is the 'excited' oxygen mass in which bulk of decay energy is deposited, η is the efficiency of transformation of decay energy deposited into [O I] doublet radiation and $L(^{56}$Co) is the luminosity of ^{56}Co which is directly proportional to the mass of ejected ^{56}Ni.

The O I luminosity of ∼1.36 × 10^{39} erg s^{-1} is obtained for SN 2012aw by integrating the flux within local minima (6214–6471 Å) and subtracting the local continuum in that region. Similarly, a value of ∼1.64 × 10^{39} erg s^{-1} is estimated for SNe 2004et at 270 d by interpolating the value using 259 and 301 d spectra taken from Sahu et al. (2006).

Assuming that in both SNe 2004et and 2012aw, η and M_{ex} are similar and given 0.83 times lower luminosity of [O I] doublet in SN 2012aw at 270 d and equal ^{56}Ni mass (Section 4.4), we derive a rough estimate of oxygen in SN 2012aw to be a factor of 0.83 lower than in SN 2004et. Considering the oxygen mass of SN 2004et as 0.8 M$_\odot$, estimated using spectral modelling of nebular phase (140 to 700 d) spectra from UV to mid-IR (Jerkstrand et al. 2012), the mass for SN 2012aw translates to be 0.66 M$_\odot$ and using nucleosynthesis yield computations in massive stars (11–40 M$_\odot$) by

Table 7. Explosion parameters of well-studied Type IIP SNe. The references for the adopted time of explosion (t_0), distance (D) and reddening $E(B-V)$ are given in Fig. 5. See Section 6.3 for further details.

Name	t_0 (245 0000+)	Δt_p (d)	t_p (d)	M_V^p (mag)	v_p ($km\,s^{-1}$)	E_0 ($\times 10^{50}$ erg)	M_{ej} ($M_\odot$)	R_0 ($R_\odot$)
SN 1999em	1475.6	92 ± 8	55 ± 4	−16.69 ± 0.01	3512 ± 122	7 ± 2	11 ± 3	399 ± 54
SN 1999gi	1522.3	97 ± 8	58 ± 4	−16.26 ± 0.02	2746 ± 217	4 ± 1	10 ± 3	421 ± 99
SN 2004et	3270.5	87 ± 8	63 ± 4	−17.01 ± 0.03	3630 ± 142	6 ± 2	9 ± 2	591 ± 90
SN 2012aw	6002.6	96 ± 11	57 ± 6	−16.67 ± 0.03	3631 ± 200	9 ± 3	14 ± 5	337 ± 67

Woosley & Weaver (1995) corresponds to the main-sequence solar metallicity stellar mass of 14 to 15 $M_\odot$.

The comparison with O I luminosity of SN 1987A [a value of $\sim 2.1 \times 10^{39}$ erg s^{-1} is estimated by interpolating values obtained at 197 and 338 d using spectrum taken from Pun et al. (1995)] with SN 2012aw indicates the mass of oxygen in SN 2012aw to be a factor of 0.84 lower than in SN 2004et. Considering the oxygen mass determinations of SN 1987A in range 1.2–1.5 $M_\odot$ (Li & McCray 1992; Chugai 1994; Kozma & Fransson 1998), the mass range for SN 2012aw translates to 1.0–1.26 $M_\odot$ and using nucleosynthesis computations this corresponds to the main-sequence solar metallicity stellar mass of 17–19 $M_\odot$ (Woosley & Weaver 1995).

The minimum mass of oxygen can also be obtained independently using the equation (Uomoto 1986):

$$M_{O\,i} = 10^8 F_{O\,i} D^2 e^{2.28/T_4},$$

where $F_{O\,i}$ is the O I doublet flux in units of erg s^{-1}, D is the distance to the SN in units of Mpc and T_4 is the temperature in units of 10^4 K. From Liu & Dalgarno (1995), the O temperature of SN 1987A at 300 d was ∼4200 K. Assuming a similar O temperature for SN 2012aw at a comparable epoch, the oxygen mass for SN 2012aw was calculated for temperatures in the range 3500–4500 K as 0.18–0.77 $M_\odot$ with the corresponding minimum main-sequence masses in the range 11–16 $M_\odot$.

6.3 Explosion parameters

Accurate estimates of explosion parameters of Type IIP SNe require detailed hydrodynamical modelling of their bolometric light curve (e.g. Bersten et al. 2011, references therein) which is beyond the scope of this paper; however, the analytical relations connecting the observed parameters (viz. the duration of the plateau Δt_p, the mid-plateau absolute magnitude M_V^p and the mid-plateau photospheric velocity v_p) with physical parameters of the explosion (viz. the energy of the explosion E_0, the radius of progenitor star R_0 and the mass of the ejected matter M_{ej}) do exist (Arnett 1980). Litvinova & Nadezhin (1983, 1985, LN85) made numerical calibration of these relations for a wide range of observables using a grid of hydrodynamical models for different values of E_0, R_0 and M_{ej}. The applicability of such a relation has been questioned as the ejected masses derived using LN85 relations for a large set of IIP SNe (14–56 $M_\odot$ by Hamuy 2003; 10–30 $M_\odot$ by Nadyozhin 2003) are consistently higher than those obtained using direct pre-SN imaging (6–15 $M_\odot$ by Smartt et al. 2009). Some of the problems lie in the lack of good quality data, simplified physical assumptions and non-inclusion of nickel heating effects (e.g. see Bersten et al. 2011); however, these relations are still useful in comparing the relative explosion properties of IIP SNe.

For the sake of estimating observed parameters for SN 2012aw and comparing with other SNe, having similar light-curve/spectra behaviour, in a consistent manner, we consider nearby normal Type IIP SNe 1999em, 1999gi and 2004et for which the distances, reddening and time of explosions are known quite accurately and all of these have good photometric and spectroscopic observations during the plateau phase. The value of Δt_p to be determined using M_V light curve (see Fig. 5) in a manner described by Nadyozhin (2003) is non-trivial; however, a plateau duration of ∼100 d is clearly apparent for all the four SNe. As noted in Section 4.1, the V-band light curve of sample SNe peaks between 10 and 16 d post-explosion and show a slow linear decline until ∼110 d, we have therefore fitted a straight line to the linear part of the plateau to estimate the phases at which the slope changes significantly by including two consecutive points at the ends. The value of Δt_p determined in this way and the phase t_p corresponding to mid-point are given in Table 7. Furthermore, at t_p, we obtain both the value of M_V^p by linear interpolation (data from Fig. 5) and the value of v_p by third-order polynomial interpolation of v_{pha} values shown in Fig. 18, which were determined by absorption minima to Fe II lines. The explosion parameters determined in this way are listed in Table 7 and it can be seen that the properties of SN 2012aw are very much similar to SNe 1999gi, 1999em and 2004et.

The value of E_0 is close to the standard energy of SNe explosion ($\sim 10^{51}$ erg) and the pre-SN radius is consistent with that of Galactic red supergiant stars measured observationally by Levesque et al. (2005). The value of M_{ej} lies in the range 9–14 $M_\odot$ and accounting for a total of 2 $M_\odot$ including mass of neutron star (a possible endpoint of IIP SNe) and the mass-loss during red supergiant phase, this corresponds to a main-sequence mass of 11–16 $M_\odot$. It is noted that using Sc II 4670 Å line for the photospheric velocities in our computation provides lower values of ejected masses. These values are consistent with the values determined using direct imaging of pre-SN stars (Smartt et al. 2009). Furthermore, it is seen that all these SNe have similar properties in terms of explosion energy, ejected mass and the radius of pre-SN star and considering uncertainty in estimating Δt_p and v_p, it is difficult to find any trend in their relative explosion parameters, and we need a larger sample of nearby IIP SNe having good quality data and a uniform approach to verify the applicability of analytical relations. For example, we note that using the LN85 relations, Maguire et al. (2010) derived the value of M_{ej} for SNe 1999em, 1999gi and 2004et in the range 14–21 $M_\odot$ and they employed the plateau duration in the range 110–120 d and the photospheric velocity derived from Sc II 6246 Å line.

7 CONCLUSIONS

We present new *UBVRI* photometric and low-resolution spectroscopic observations of an SN event SN 2012aw which occurred in the outskirt of a nearby (9.9 ± 0.1 Mpc) galaxy M95. The time of explosion is constrained with an accuracy of a day and the position of SN in the galaxy is consistent with being located in a solar metallicity region. The photometric observations are presented at 45 phases during 4 to 269 d while the low-resolution (6–12 Å)

spectroscopic observations are presented at 14 phases during 7 to 270 d. Employing the high-resolution spectrum of Na I D region and the early time photometric SED, the value of $E(B-V)$ is constrained quite accurately to be 0.07 ± 0.01 mag.

The light-curve characteristics of apparent magnitudes, colours and the bolometric luminosity is found to have striking similarity with the archetypal IIP SNe 1999em, 1999gi and 2004et; all showing the plateau duration of about 100 d. For all these SNe, the light curve in V band rises to a peak between 10 and 16 d post-explosion and then follows slow decline during the plateau phase. However, for SN 2012aw our early time observations clearly detect minima in the light curve of V, R and I bands near 32 d after explosion and this we suggest to be an observational evidence seen for the first time in any Type IIP SNe, for the emergence of flux due to onset of recombination phase. The value of the mid-plateau M_V is -16.67 ± 0.04 for SN 2012aw lies in between the bright IIP SNe (~ -18 mag; e.g. 2007od, 2009bw) and the subluminous IIP SNe (~ -15 mag; e.g. 2005cs, 1997D). Employing nebular phase bolometric luminosity, we estimate mass of ^{56}Ni to be 0.06 ± 0.01, similar to the SNe 1999em, 2004et and 1987A.

The presence and evolution of prominent optical spectral features show striking similarity with the IIP SNe 1999em, 1999gi and 2004et. We have identified and studied the evolution of spectral features using the SYNOW modelling. Similar to SNe 1999em and 1999gi, two peculiar HV components associated with the regular Hβ and He I P-Cygni features are seen in the early (7 and 8 d) spectra, indicating early interaction of ejecta with the CSM. However, these absorption features are consistent with being reproduced by invoking N II lines in the SYNOW modelling. During 55 to 104 d, the absorption profiles of Hβ and Hα are broadened and they only fit by invoking HV components showing signs of ejecta interaction with CSM during the late plateau phase. We note that interaction scenario is consistent with the detection of SN 2012aw in X-rays (0.1–10 keV) during 4 to 6 d (Immler & Brown 2012) and at 21 GHz radio observations during 8 to 14 d (Stockdale et al. 2012; Yadav et al. 2012).

The velocity of Hα and [O I] doublet line-emitting regions in the nebular phase spectrum at 270 d is found to be similar to that observed for SNe 1999em and 2004et; and the line profile shapes are consistent with being originated from spherically symmetric regions, showing no signs of dust formation.

The value and evolution of the photospheric velocity as derived using Fe II lines is found to be similar to SN 2004et, but about $\sim$600 km s^{-1} higher than that of SNe 1999em and 1999gi at similar epochs. This trend was more apparent in the line velocities of Hα and Hβ. The comparison of the photospheric velocity at 15 d with that derived using radiation-hydrodynamics simulations of IIP SNe by Dessart et al. (2010) indicate that the energy of explosion is about 1–2 $\times$ 10^{51} erg and this coupled with the velocity of [O I] line suggests an upper mass limit of 15 $M_\odot$ for a non-rotating solar metallicity progenitor star. We further constrain, the progenitor mass by comparing [O I] emission luminosity with the SNe 2004et and 1987A and we find that the core of oxygen mass was smaller than that of SNe 2004et and 1987A, and assuming similar physical conditions, we derive mass of progenitor star to be about 14–15 $M_\odot$.

We have also estimated explosion parameters using analytical relations of LN85 for SNe 1999gi, 1999em, 2004et and 2012aw; all having good coverage of photometric and spectroscopic data during the plateau phase, in a consistent manner. We find no trend in relative parameters but ensemble parameters are found to be consistent with those expected for a normal luminosity IIP SNe, i.e. the explosion energy is consistent with 1 $\times$ 10^{51} erg, the pre-SN radius is similar to what is expected from a red supergiant star and the mass of progenitor lies between 11 and 16 $M_\odot$.

SN 2012aw along with Type IIP SNe 1999gi, 1999em and 2004et form a golden sample to test results from radiation hydrodynamical simulations.

ACKNOWLEDGEMENTS

We thank all the observers at Aryabhatta Research Institute of Observational Sciences (ARIES) who provided their valuable time and support for the observations of this event. We are thankful to the observing staff and technical assistants of ARIES 1.3 m Devasthal telescope and we also express our thanks to 2 m IGO, 2 m HCT telescope staff for their kind cooperation in observation of SN 2012aw. We gratefully acknowledge the services of the NASA ADS and NED data bases and also the online SN spectrum archive (SUSPECT) which are used to access data and references in this paper. We thank K. Maguire for providing late spectroscopic data of SN 2004et. We would also like to thank the anonymous referee for the comments and suggestions which helped in improvement of this manuscript.

REFERENCES

Arcavi I. et al., 2012, ApJ, 756, L30
Arnett W. D., 1980, ApJ, 237, 541
Arnett D., 1996, Supernovae and Nucleosynthesis: An Investigation of the History of Matter from the Big Bang to the Present. Princeton Univ. Press, Princeton, NJ
Asplund M., Grevesse N., Sauval A. J., Scott P., 2009, ARA&A, 47, 481
Barbon R., Benetti S., Rosino L., Cappellaro E., Turatto M., 1990, A&A, 237, 79
Baron E. et al., 2000, ApJ, 545, 444
Baron E., Nugent P. E., Branch D., Hauschildt P. H., 2004, ApJ, 616, L91
Bayless A. J. et al., 2013, ApJ, 764, L13
Bersten M. C., Benvenuto O., Hamuy M., 2011, ApJ, 729, 61
Bose S., Kumar B., 2013, in Ray A., McGray D., eds, IAU Symp. 296, Supernova environmental impacts. Cambridge Univ. Press, Cambridge, in press
Branch D. et al., 2002, ApJ, 566, 1005
Burrows A., 2013, Rev. Mod. Phys., 85, 245
Cardelli J. A., Clayton G. C., Mathis J. S., 1989, ApJ, 345, 245
Chakraborty P., Das1 H. K., Tandon S. N., 2005, Bull. Astron. Soc. India, 33, 513
Chugai N. N., 1988, Sov. Astron. Lett., 14, 334
Chugai N. N., 1994, ApJ, 428, L17
Cowen D. F., Franckowiak A., Kowalski M., 2010, Astropart. Phys., 33, 19
Dessart L., Hillier D. J., 2005a, A&A, 437, 667
Dessart L., Hillier D. J., 2005b, in Humphreys R., Stanek K., eds, ASP Conf. Ser. Vol. 332, The Fate of the Most Massive Stars. Astron. Soc. Pac., San Francisco, p. 415
Dessart L., Hillier D. J., 2006, A&A, 447, 691
Dessart L., Livne E., Waldman R., 2010, MNRAS, 408, 827
Elmhamdi A. et al., 2003, MNRAS, 338, 939
Fagotti P. et al., 2012, Cent. Bur. Electron. Telegrams, 3054, 1
Filippenko A. V., 1997, ARA&A, 35, 309
Fisher A., Branch D., Nugent P., Baron E., 1997, ApJ, 481, L89
Fisher A., Branch D., Hatano K., Baron E., 1999, MNRAS, 304, 67
Fraser M. et al., 2011, MNRAS, 417, 1417
Fraser M. et al., 2012, ApJ, 759, L13
Freedman W. L. et al., 2001, ApJ, 553, 47
Fukugita M., Shimasaku K., Ichikawa T., 1995, PASP, 107, 945
Gandhi P. et al., 2013, ApJ, 767, 166
Gupta R. et al., 2002, Bull. Astron. Soc. India, 30, 745
Hamuy M., 2003, ApJ, 582, 905

Hamuy M., Suntzeff N. B., 1990, AJ, 99, 1146
Hamuy M., Suntzeff N. B., Heathcote S. R., Walker A. R., Gigoux P., Phillips M. M., 1994, PASP, 106, 566
Hanuschik R. W., Dachs J., 1987, A&A, 182, L29
Heger A., Fryer C. L., Woosley S. E., Langer N., Hartmann D. H., 2003, ApJ, 591, 288
Henden A., Krajci T., Munari U., 2012, Inf. Bull. Var. Stars, 6024, 1
Horne K., 1986, PASP, 98, 609
Immler S., Brown P. J., 2012, Astron. Telegram, 3995, 1
Inserra C. et al., 2011, MNRAS, 417, 261
Inserra C., Baron E., Turatto M., 2012a, MNRAS, 422, 1178
Inserra C. et al., 2012b, MNRAS, 422, 1122
Itoh R., Ui T., Yamanaka M., 2012, Cent. Bur. Electron. Telegrams, 3054, 2
Janka H.-T., 2012, Annu. Rev. Nucl. Part. Sci., 62, 407
Jeffery D. J., Branch D., 1990, in Wheeler J. C., Piran T., Weinberg S., eds, Supernovae, Jerusalem Winter School for Theoretical Physics. World Scientific Publishing Co., Singapore, p. 149
Jerkstrand A., Fransson C., Maguire K., Smartt S., Ergon M., Spyromilio J., 2012, A&A, 546, A28
Jordi K., Grebel E. K., Ammon K., 2006, A&A, 460, 339
Kasen D., Woosley S. E., 2009, ApJ, 703, 2205
Kochanek C. S., Khan R., Dai X., 2012, ApJ, 759, 20
Kozma C., Fransson C., 1998, ApJ, 497, 431
Landolt A. U., 2009, AJ, 137, 4186
Leonard D. C. et al., 2002a, PASP, 114, 35
Leonard D. C. et al., 2002b, AJ, 124, 2490
Leonard D. C., Pignata G., Dessart L., Hillier D., Horst C., Fedrow J. M., Brewer L., 2012, Astron. Telegram, 4033, 1
Levesque E. M., Massey P., Olsen K. A. G., Plez B., Josselin E., Maeder A., Meynet G., 2005, ApJ, 628, 973
Li H., McCray R., 1992, ApJ, 387, 309
Litvinova I. I., Nadezhin D. K., 1983, Ap&SS, 89, 89
Litvinova I. Y., Nadezhin D. K., 1985, Sov. Astron. Lett., 11, 145
Liu W., Dalgarno A., 1995, ApJ, 454, 472
Maguire K. et al., 2010, MNRAS, 404, 981
Maguire K. et al., 2012, MNRAS, 420, 3451
Misra K., Pooley D., Chandra P., Bhattacharya D., Ray A. K., Sagar R., Lewin W. H. G., 2007, MNRAS, 381, 280
Munari U., Vagnozzi A., Castellani F., 2012, Cent. Bur. Electron. Telegrams, 3054, 3
Nadyozhin D. K., 2003, MNRAS, 346, 97
Oke J. B., 1990, AJ, 99, 1621
Pastorello A. et al., 2002, MNRAS, 333, 27
Pastorello A. et al., 2004, MNRAS, 347, 74
Pastorello A. et al., 2009, MNRAS, 394, 2266
Pastorello A. et al., 2012, A&A, 537, A141
Patat F., Barbon R., Cappellaro E., Turatto M., 1994, A&A, 282, 731
Paturel G., Petit C., Prugniel Ph., Theureau G., Rousseau J., Brouty M., Dubois P., Cambrésy L., 2003, A&A, 412, 45
Pilyugin L. S., Thuan T. X., Vílchez J. M., 2006, MNRAS, 367, 1139
Poznanski D., Ganeshalingam M., Silverman J. M., Filippenko A. V., 2011, MNRAS, 415, L81
Poznanski D., Nugent P. E., Ofek E. O., Gal-Yam A., Kasliwal M. M., 2012a, Astron. Telegram, 3996, 1
Poznanski D., Prochaska J. X., Bloom J. S., 2012b, MNRAS, 426, 1465
Pun C. S. J. et al., 1995, ApJS, 99, 223
Quimby R. M., Wheeler J. C., Höflich P., Akerlof C. W., Brown P. J., Rykoff E. S., 2007, ApJ, 666, 1093
Roy R. et al., 2011, ApJ, 736, 76
Russell D. G., 2002, ApJ, 565, 681
Sagar R., Kumar B., Omar A., Joshi Y. C., 2012, in Annapurni S., Sumedh A., eds, ASI Conf. Ser. Vol. 4, Recent Advances in Star Formation: Observation and Theory. Astron. Soc. India, p. 173
Sagar R., Kumar B., Omar A., 2013, preprint (arXiv:1304.0235)
Sahu D. K., Anupama G. C., Srividya S., Muneer S., 2006, MNRAS, 372, 1315
Schlegel D. J., Finkbeiner D. P., Davis M., 1998, ApJ, 500, 525
Siviero A. et al., 2012, Cent. Bur. Electron. Telegrams, 3054, 4
Smartt S. J., Eldridge J. J., Crockett R. M., Maund J. R., 2009, MNRAS, 395, 1409
Stalin C. S., Hegde M., Sahu D. K., Parihar P. S., Anupama G. C., Bhatt B. C., Prabhu T. P., 2008, Bull. Astron. Soc. India, 36, 111
Stetson P. B., 1987, PASP, 99, 191
Stetson P. B., 1992, J. R. Astron. Soc. Can., 86, 71
Stockdale C. J. et al., 2012, Astron. Telegram, 4012, 1
Takáts K., Vinkó J., 2012, MNRAS, 419, 2783 (TV12)
Tsvetkov D. Y., Goranskij V., Pavlyuk N., 2008, Perem. Zvezdy, 28, 8
Turatto M., Benetti S., Cappellaro E., 2003, in Hillebrandt W., Leibundgut B., eds, From Twilight to Highlight: The Physics of Supernovae. Springer-Verlag, Berlin, p. 200
Uomoto A., 1986, ApJ, 310, L35
Utrobin V. P., 2007, A&A, 461, 233
Utrobin V. P., Chugai N. N., 2009, A&A, 506, 829
Utrobin V. P., Chugai N. N., 2011, A&A, 532, A100
van Dokkum P. G., 2001, PASP, 113, 1420
Van Dyk S. D. et al., 2012, ApJ, 756, 131
Vollmann K., Eversberg T., 2006, Astron. Nachr., 327, 862
Woosley S. E., Weaver T. A., 1995, ApJS, 101, 181
Yadav N., Chakraborti S., Ray A., 2012, Astron. Telegram, 4010, 1

This paper has been typeset from a TEX/LATEX file prepared by the author.